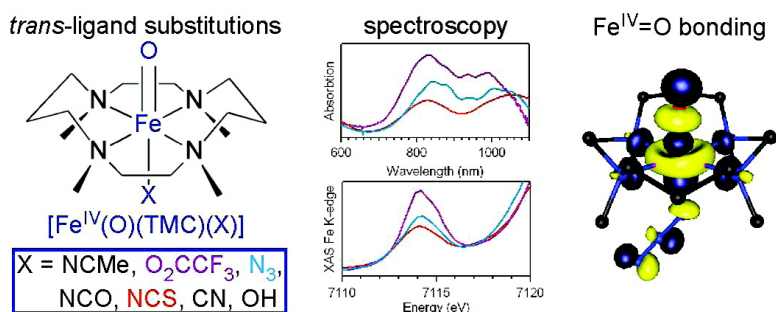**Article**

Axial Ligand Effects on the Geometric and Electronic Structures of Nonheme Oxoiron(IV) Complexes

Timothy A. Jackson, Jan-Uwe Rohde, Mi Sook Seo, Chivukula V. Sastri, Raymond DeHont, Audria Stubna, Takehiro Ohta, Teizo Kitagawa, Eckard Mu#nck, Wonwoo Nam, and Lawrence Que Jr.

trans-ligand substitutions   spectroscopy   Fe^{IV}=O bonding

[Fe^{IV}(O)(TMC)(X)]

X = NCMe, O$_2$CCF$_3$, N$_3$, NCO, NCS, CN, OH

More About This Article

Additional resources and features associated with this article are available within the HTML version:

- Supporting Information
- Links to the 2 articles that cite this article, as of the time of this article download
- Access to high resolution figures
- Links to articles and content related to this article
- Copyright permission to reproduce figures and/or text from this article

View the Full Text HTML

Axial Ligand Effects on the Geometric and Electronic Structures of Nonheme Oxoiron(IV) Complexes

Timothy A. Jackson,[†,‡] Jan-Uwe Rohde,[†,#] Mi Sook Seo,[§] Chivukula V. Sastri,[§] Raymond DeHont,[||] Audria Stubna,[||] Takehiro Ohta,[⊥] Teizo Kitagawa,[⊥] Eckard Münck,*,[||] Wonwoo Nam,*,[§] and Lawrence Que, Jr.*,[†]

Department of Chemistry and Center for Metals in Biocatalysis, 207 Pleasant Street S.E., University of Minnesota, Minneapolis, Minnesota 55455, Department of Chemistry, Division of Nano Sciences, and Center for Biomimetic Systems, Ewha Womans University, Seoul 120-750, Korea, Okazaki Institute for Integrative Bioscience, National Institutes of Natural Sciences, Okazaki, Aichi 444-8787, Japan, and Department of Chemistry, Carnegie Mellon University, Pittsburgh, Pennsylvania 15213

Received March 29, 2008; E-mail: larryque@umn.edu; wwnam@ewha.ac.kr; emunck@cmu.edu

Abstract: A series of complexes $[Fe^{IV}(O)(TMC)(X)]^+$ (where $X = OH^-$, $CF_3CO_2^-$, N_3^-, NCS^-, NCO^-, and CN^-) were obtained by treatment of the well-characterized nonheme oxoiron(IV) complex $[Fe^{IV}(O)(TMC)(NCMe)]^{2+}$ (TMC = tetramethylcyclam) with the appropriate NR_4X salts. Because of the topology of the TMC macrocycle, the $[Fe^{IV}(O)(TMC)(X)]^+$ series represents an extensive collection of $S = 1$ oxoiron(IV) complexes that only differ with respect to the ligand trans to the oxo unit. Electronic absorption, Fe K-edge X-ray absorption, resonance Raman, and Mössbauer data collected for these complexes conclusively demonstrate that the characteristic spectroscopic features of the $S = 1$ $Fe^{IV}=O$ unit, namely, (i) the near-IR absorption properties, (ii) X-ray absorption pre-edge intensities, and (iii) quadrupole splitting parameters, are strongly dependent on the identity of the trans ligand. However, on the basis of extended X-ray absorption fine structure data, most $[Fe^{IV}(O)(TMC)(X)]^+$ species have Fe=O bond lengths similar to that of $[Fe^{IV}(O)(TMC)(NCMe)]^{2+}$ (1.66 ± 0.02 Å). The mechanisms by which the trans ligands perturb the $Fe^{IV}=O$ unit were probed using density functional theory (DFT) computations, yielding geometric and electronic structures in good agreement with our experimental data. These calculations revealed that the trans ligands modulate the energies of the Fe=O σ- and π-antibonding molecular orbitals, causing the observed spectroscopic changes. Time-dependent DFT methods were used to aid in the assignment of the intense near-UV absorption bands found for the oxoiron(IV) complexes with trans N_3^-, NCS^-, and NCO^- ligands as X^--to-$Fe^{IV}=O$ charge-transfer transitions, thereby rationalizing the resonance enhancement of the ν(Fe=O) mode upon excitation of these chromophores.

1. Introduction

Iron plays a number of fundamental roles in biological systems, but perhaps no role has attracted greater attention among chemists than that of oxygen activation.[1−4] Certain classes of both heme and nonheme iron enzymes harness the oxidizing power of O_2 to perform vital biological transformations, such as the hydroxylation of unactivated C−H bonds.

For the heme systems, it is generally accepted that the active oxidant for these reactions is the so-called compound I intermediate, an oxoiron(IV) unit coupled to a porphyrin cation radical.[4] For certain classes of O_2-activating mononuclear nonheme iron systems, it has been assumed for several years that an oxoiron(IV) center is the active oxidant.[1] Recent work has established the presence of such intermediates in the catalytic cycles of several nonheme iron enzymes,[5] namely, the α-ketoglutarate-dependent taurine/α-ketoglutarate dioxygenase (TauD),[6−9] prolyl-4-hydroxylase,[10] and the halo-

† University of Minnesota.
‡ Current address: Department of Chemistry, University of Kansas, Lawrence, KS 66045.
# Current address: Department of Chemistry, University of Iowa, Iowa City, IA 52242.
§ Ewha Womans University.
|| Carnegie Mellon University.
⊥ National Institutes of Natural Sciences.

(1) Costas, M.; Mehn, M. P.; Jensen, M. P.; Que, L., Jr. *Chem. Rev.* **2004**, *104*, 939–986.
(2) Solomon, E. I.; Brunold, T. C.; Davis, M. I.; Kemsley, J. N.; Lee, S. K.; Lehnert, N.; Neese, F.; Skulan, A. J.; Yang, Y. S.; Zhou, J. *Chem. Rev.* **2000**, *100*, 235–349.
(3) Wallar, B. J.; Lipscomb, J. D. *Chem. Rev.* **1996**, *96*, 2625–2658.
(4) Sono, M.; Roach, M. P.; Coulter, E. D.; Dawson, J. H. *Chem. Rev.* **1996**, *96*, 2841–2887.

(5) Krebs, C.; Galonić Fujimori, D.; Walsh, C. T.; Bollinger, J. M., Jr. *Acc. Chem. Res.* **2007**, *40*, 484–492.
(6) Price, J. C.; Barr, E. W.; Tirupati, B.; Bollinger, J. M., Jr.; Krebs, C. *Biochemistry* **2003**, *42*, 7497–7508.
(7) Price, J. C.; Barr, E. W.; Glass, T. E.; Krebs, C.; Bollinger, J. M., Jr. *J. Am. Chem. Soc.* **2003**, *125*, 13008–13009.
(8) Riggs-Gelasco, P. J.; Price, J. C.; Guyer, R. G.; Brehm, J. H.; Barr, E. W.; Bollinger, J. M., Jr.; Krebs, C. *J. Am. Chem. Soc.* **2004**, *126*, 8108–8109.
(9) Proshlyakov, D. A.; Henshaw, T. F.; Monterosso, G. R.; Ryle, M. J.; Hausinger, R. P. *J. Am. Chem. Soc.* **2004**, *126*, 1022–1023.
(10) Hoffart, L. M.; Barr, E. W.; Guyer, R. G.; Bollinger, J. M., Jr.; Krebs, C. *Proc. Natl. Acad. Sci. U.S.A.* **2006**, *103*, 14738–14743.
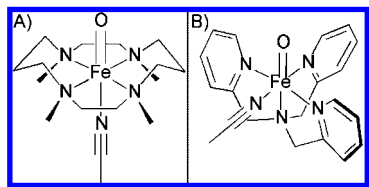
Figure 1. Representations of the molecular structures of [Fe^{IV}(O)(TMC)-(NCMe)]$^{2+}$ (A) and [Fe^{IV}(O)(TPA)(NCMe)]$^{2+}$ (B) based on X-ray crystallographic data[18] and density functional theory computations,[25] respectively.

genase CytC3,[11] as well as the tetrahydropterin-dependent tyrosine hydroxylase.[12] These oxoiron(IV) species all have $S = 2$ ground states, and the Fe=O bond lengths of the TauD and CytC3 intermediates were determined to be 1.61–1.62 Å by analysis of extended X-ray absorption fine structure (EXAFS) data.[8,13] The observation of oxoiron(IV) intermediates in four different nonheme iron enzymes greatly strengthens the notion that the Fe^{IV}=O unit is a common oxidant.

Because of its occurrence in the catalytic cycles of nonheme iron enzymes, as well as the possible utility of analogous biomimetic oxidants in hydroxylation and O-atom transfer reactions,[14–16] the oxoiron(IV) unit has long been a target of the modeling community. Within the last several years, synthetic efforts yielded a variety of mononuclear nonheme oxoiron(IV) complexes,[16–23] most of which were found to have $S = 1$ ground states.[24] Two X-ray crystal structures featuring mononuclear Fe^{IV}=O units were reported,[18,21] with a representation based on that of [Fe^{IV}(O)(TMC)(NCMe)]$^{2+}$ (where TMC = 1,4,8,11-tetramethyl-1,4,8,11-tetraazacyclotetradecane) shown in Figure 1A. These structures have unequivocally established the metrical parameters of the oxoiron(IV) center, the hallmark of which is a short Fe=O distance of ~1.64–1.65 Å. Additionally, the spectroscopic properties of these complexes were characterized in detail, revealing a number of signatures of the $S = 1$

oxoiron(IV) unit, including (i) near-infrared (NIR) absorption bands with low intensities ($\varepsilon \leq 400$ M^{-1} cm^{-1}), (ii) Fe K-edge pre-edge transitions with large areas (~20–30 units relative to the edge jump), and (iii) low Mössbauer isomer shift values ($\delta = -0.04$–0.19 mm/s).[16]

One of the advantages of studying synthetic oxoiron(IV) complexes is that, in principle, the coordination sphere around the Fe=O unit can be systematically modulated to determine how the local coordination geometry governs electronic structure and reactivity. This can be most easily done for the oxoiron(IV) complexes supported by the TMC and tris(pyridylmethyl)amine (TPA) ligands, as these tetradentate ligands provide labile coordination sites trans and cis, respectively, to the oxo group (Figure 1). A systematic study of a series of [Fe^{IV}(O)(T-PA)(X)]$^{2+/+}$ complexes (where X = MeCN, CF$_3$CO$_2^-$, Cl$^-$, and Br$^-$) revealed that cis substitutions have only a minor effect on (i) the Fe=O bond length, which in all cases was determined by EXAFS analyses to be ~1.65 Å, (ii) the quadrupole splitting ($\Delta E_Q = 0.93 \pm 0.02$ mm/s for all complexes), and (iii) the X-ray absorption pre-edge area (25 ± 2 units).[25] Thus, other than causing a shift in the NIR absorption band,[25] it would appear that cis substitutions do not markedly affect the signature features of the $S = 1$ Fe=O unit.

In contrast, [Fe^{IV}(O)(TMC)(X)]$^{2+/+}$ (**1**-X, where X = MeCN, CF$_3$CO$_2^-$, N$_3^-$, and NCS$^-$)[18,26–28] and the closely related complex [Fe^{IV}(O)(TMCS)]$^+$ (**1′**-SR),[29] which has a tethered thiolate ligand that can bind trans to the oxo group, exhibit a remarkable range of properties. For instance, whereas the parent complex **1**-NCMe displays only modest absorption features in the NIR spectral region, the **1**-N$_3$ and **1**-NCS complexes show intense charge-transfer features at ~400 nm.[28] These chromophores permitted the use of resonance Raman (RR) spectroscopy to determine the frequency of the Fe=O stretching mode of these complexes.[28] In terms of structural variation, EXAFS data revealed that the presence of a *trans*-thiolate group gives rise to a longer Fe=O distance of 1.70 Å, an elongation of 0.05 Å compared to **1**-NCMe.[30] A recent study also showed that the reactivity pattern of the oxoiron(IV) unit is highly dependent on the trans ligand.[27] For example, **1**-NCMe is a more reactive oxygen atom transfer agent to triphenylphosphine than **1′**-SR by roughly 300-fold, whereas **1′**-SR is a more potent hydrogen atom abstraction agent over **1**-NCMe by a factor of ~50, when dihydroanthracene is used as substrate.[27] Thus, the chemical nature of the trans ligand governs whether the oxoiron(IV) unit is a more effective two-electron (oxygen atom transfer) or one-electron (hydrogen atom abstraction) oxidant.

In this article, we describe the spectroscopic and structural properties of seven oxoiron(IV) complexes that differ only with respect to the ligand trans to the oxo group. By using electronic absorption, X-ray absorption, Mössbauer, and resonance Raman

(11) Galonic, D. O.; Barr, E. W.; Walsh, C. T.; Bollinger, J. M., Jr.; Krebs, C. *Nat. Chem. Biol.* **2007**, *3*, 113–116.
(12) Eser, B. E.; Barr, E. W.; Frantom, P. A.; Saleh, L.; Bollinger, J. M., Jr.; Krebs, C.; Fitzpatrick, P. F. *J. Am. Chem. Soc.* **2007**, *40*, 11334–11335.
(13) Galonic Fujimori, D.; Barr, E. W.; Matthews, M. L.; Koch, G. M.; Yonce, J. R.; Walsh, C. T.; Bollinger, J. M., Jr.; Krebs, C.; Riggs-Gelasco, P. J. *J. Am. Chem. Soc.* **2007**, *129*, 13408–13409.
(14) Nam, W. *Acc. Chem. Res.* **2007**, *40*, 522–531.
(15) Kaizer, J.; Klinker, E. J.; Oh, N. Y.; Rohde, J.-U.; Song, W. J.; Stubna, A.; Kim, J.; Münck, E.; Nam, W.; Que, L., Jr. *J. Am. Chem. Soc.* **2004**, *126*, 472–473.
(16) Shan, X.; Que, L., Jr. *J. Inorg. Biochem.* **2006**, *100*, 421–433.
(17) Que, L., Jr. *Acc. Chem. Res.* **2007**, *40*, 493–500.
(18) Rohde, J.-U.; In, J.-H.; Lim, M. H.; Brennessel, W. W.; Bukowski, M. R.; Stubna, A.; Münck, E.; Nam, W.; Que, L., Jr. *Science* **2003**, *299*, 1037–1039.
(19) Lim, M. H.; Rohde, J. U.; Stubna, A.; Bukowski, M. R.; Costas, M.; Ho, R. Y. N.; Munck, E.; Nam, W.; Que, L., Jr. *Proc. Natl. Acad. Sci. U.S.A.* **2003**, *100*, 3665–3670.
(20) Balland, V.; Charlot, M.-F.; Banse, F.; Girerd, J.-J.; Mattioli, T. A.; Bill, E.; Bartoli, J.-F.; Battioni, P.; Mansuy, D. *Eur. J. Inorg. Chem.* **2004**, 301–308.
(21) Klinker, E. J.; Kaizer, J.; Brennessel, W. W.; Woodrum, N. L.; Cramer, C. J.; Que, L., Jr. *Angew. Chem., Int. Ed.* **2005**, *44*, 3690–3694.
(22) Grapperhaus, C. A.; Mienert, B.; Bill, E.; Weyhermuller, T.; Wieghardt, K. *Inorg. Chem.* **2000**, *39*, 5306–5317.
(23) Martinho, M.; Banse, F.; Bartoli, J.-F.; Mattioli, T. A.; Battioni, P.; Horner, O.; Bourcier, S.; Girerd, J.-J. *Inorg. Chem.* **2005**, *44*, 9592–9596.
(24) An exception is the aqueous oxoiron(IV) complex obtained by Bakac and co-workers that has an $S = 2$ spin ground state. See: Pestovsky, O.; Stoian, S.; Bominaar, E. L.; Shan, X.; Munck, E.; Que, L., Jr.; Bakac, A. *Angew. Chem., Int. Ed.* **2005**, *44*, 6871–6874.

(25) Rohde, J.-U.; Stubna, A.; Bominaar, E. L.; Münck, E.; Nam, W.; Que, L., Jr. *Inorg. Chem.* **2006**, *45*, 6435–6445.
(26) Rohde, J.-U.; Que, L., Jr. *Angew. Chem., Int. Ed.* **2005**, *44*, 2255–2258.
(27) Sastri, C. V.; Lee, J.; Oh, K.; Lee, Y. J.; Lee, J.; Jackson, T. A.; Hirao, H.; Que, L., Jr.; Shaik, S.; Nam, W. *Proc. Natl. Acad. Sci. U.S.A.* **2007**, *104*, 19181–19186.
(28) Sastri, C. V.; Park, M. J.; Ohta, T.; Jackson, T. A.; Stubna, A.; Seo, M. S.; Lee, J.; Kim, J.; Kitagawa, T.; Münck, E.; Que, L., Jr.; Nam, W. *J. Am. Chem. Soc.* **2005**, *127*, 12494–12495.
(29) TMCS is the monoanion of 1-mercaptoethyl-4,8,11-trimethyl-1,4,8,11-tetraazacyclotetradecane.
(30) Bukowski, M. R.; Koehntop, K. D.; Stubna, A.; Bominaar, E. L.; Halfen, J. A.; Münck, E.; Nam, W.; Que, L., Jr. *Science* **2005**, *310*, 1000–1002.

spectroscopies, we more thoroughly characterized **1**-NCMe, **1**-O$_2$CCF$_3$, **1**-N$_3$, and **1**-NCS, as well as three new oxoiron(IV) complexes: [Fe^{IV}(O)(TMC)(NCO)]$^+$, [Fe^{IV}(O)(TMC)(CN)]$^+$, and [Fe^{IV}(O)(TMC)(OH)]$^+$. These data show that the nature of the trans ligand profoundly affects (i) NIR absorption features, (ii) X-ray absorption spectroscopic (XAS) pre-edge areas, (iii) Fe=O stretching frequencies, and (iv) Mössbauer properties, unlike what was observed for the cis substituted series, [Fe^{IV}(O)(TPA)(X)]$^{2+/+}$.[25] These spectroscopic studies are complemented by density functional theory (DFT) computations that allow spectroscopic changes to be correlated with differences in electronic structure. Our combined experimental and theoretical investigation reveals how the donor properties of the trans ligand modulate spectroscopic properties of the oxoiron(IV) unit and offers insights into differences in reactivity among these complexes.

2. Experimental Section

2.1. Materials and General Procedures. All reagents and solvents were purchased from commercial sources and used as received, unless otherwise noted. Solvents were dried according to published procedures[31] and distilled under argon before use. [Fe^{II}(TMC)(OTf)](OTf) and [^{57}Fe^{II}(TMC)(OTf)](OTf) were synthesized in a nitrogen atmosphere glovebox, as previously described.[18] Iodosobenzene (PhIO) was generated according to published procedures.[32]

Ligand substitution reactions were carried out by addition of the appropriate salt to 2−16 mM solutions of [Fe^{IV}(O)(TMC)(NC-Me)]$^{2+}$ (**1**-NCMe) in MeCN. Typically, 2 mL of a MeCN solution of the iron(II) precursor [Fe^{II}(TMC)(OTf)](OTf) was transferred to a cuvette that was then placed in a cryostat maintained at a desired temperature. One equivalent of PhIO (solubilized in MeOH) was subsequently added, resulting in the quantitative formation of **1**-NCMe. Upon full formation of **1**-NCMe, the appropriate NR$_4$X salt (where R = Et or Bu and X is the added anion) was added. In all cases, addition of 1−2 equiv of NR$_4$X yielded the corresponding [Fe^{IV}(O)(TMC)(X)]$^+$ (**1**-X) species in high yields (≥80%), as judged by Mössbauer data collected with ^{57}Fe-enriched samples (vide infra). Extinction coefficients were determined on the basis of the percent composition of **1**-X determined by Mössbauer spectroscopy. Samples used for tandem Mössbauer and XAS experiments were prepared by transferring an aliquot of solution (~500 μL) containing **1**-X to a precooled cup designed specifically for Mössbauer/XAS experiments. Iron concentrations in these samples were typically 10−16 mM in Fe; to carry out the Mössbauer analysis, the Fe was enriched with ^{57}Fe to achieve a final ^{57}Fe concentration of ca. 2 mM in the samples.

2.2. Physical Methods. 2.2.1. Electronic Absorption, Resonance Raman, and Mössbauer Spectroscopies. Electronic absorption spectra were collected on an HP 8453A diode-array spectrometer. Samples were maintained at a constant temperature using a Unisoku Scientific Instruments cryostat. Electrospray ionization mass spectra (ESI-MS) were collected on a Thermo Finnigan LCQ Advantage MAX quadrupole ion trap instrument, by infusing samples directly into the source at 20 μL/min using a syringe pump. The spray voltage was set at 4 kV and the capillary temperature at 70 °C. Resonance Raman spectra were obtained using a liquid nitrogen cooled CCD detector (model LN/CCD-1340 × 400PB, Princeton Instruments) attached to a 1-m single polychrometer (model MC-100DG, Ritsu Oyo Kogaku). Excitation wavelengths were provided by Kr$^+$ and Ar$^+$ lasers (Spectra Physics BeamLok 2060-RM) with ~4 mW power at the samples. All measurements

were carried out with a spinning cell (1000 rpm) at ~−20 °C. Raman shifts were calibrated with indene, and the accuracy of the peak positions of the Raman bands was ±1 cm^{-1}. Mössbauer spectra were recorded with two spectrometers, using Janis Research SuperVaritemp dewars. Isomer shifts were quoted relative to Fe metal at 298 K. All Mössbauer samples contained varying amounts of iron(II) and iron(III) contaminants (vide infra), but these contaminants did not significantly hamper the data analysis, as their spectral features could be evaluated (Figure S1) or were at Doppler velocities outside the spectral range of interest.

2.2.2. X-ray Absorption Spectroscopy. Data Collection. XAS data were collected at beamline 9−3 at the Stanford Synchrotron Radiation Laboratory (SSRL) of the Stanford Linear Accelerator Center and beamline X9B at the National Synchrotron Light Source (NSLS) of Brookhaven National Laboratory. Fe K-edge XAS data were collected for frozen solutions maintained at ~10 K over the energy range 6.9−8.0 keV, as previously described.[33−35] An iron foil spectrum was measured simultaneously for internal energy calibration using the first inflection point of the K-edge energy (7112.0 eV). Data were obtained as fluorescence excitation spectra using a solid-state germanium detector (Canberra).

2.2.3. Data Analysis. Data reduction, averaging, and normalization were performed using the program EXAFSPAK.[36] Background corrections were also performed using EXAFSPAK, as previously described.[37] The intensity and energy of pre-edge features for the **1**-X complexes were determined according to a pre-edge fitting protocol using the program SSEXAFS,[33,38] which we previously used for high-valent species.[25,35,37,39] The edge was modeled as an integral of a 75% Gaussian and 25% Lorentzian peak; the pre-edge peak was modeled as a Gaussian function whose height, position, and width (at half-height) were refined. Pre-edge peak areas are reported as percent of the Fe K-edge jump. EXAFS refinement was carried out on $k^3\chi(k)$ data (see Figure S2 for raw data), using phase and amplitude functions obtained from FEFF, version 6. EXAFS data fittings were performed by initial refinement using the back-transformation ranges indicated in Tables S1 and S2. For each fit, the parameters r and σ^2 were optimized, while n was kept fixed. n was systematically varied in integer steps. Unfiltered data were subsequently fit. The goodness of fit was assessed by F, where $F = \Sigma(\chi_{calcd} - \chi_{expt})^2/N$, and N is the number of data points. The threshold energy, E_0, in electronvolts ($k = 0$ point), was maintained at a common, variable value for all shells of a given fit. More technical details of our fitting procedures are described in Supporting Information.

2.3. Computations. 2.3.1. DFT Geometry Optimizations. The structure of [Fe^{IV}(O)(TMC)(NCMe)]$^{2+}$ determined by X-ray crystallography[18] was used as starting point for all DFT energy minimizations. Models of [Fe^{IV}(O)(TMC)(X)]$^+$ were derived by replacing the NCMe ligand with the appropriate X ligand (where X = OH$^-$, N$_3^-$, NCS$^-$, NCO$^-$, CN$^-$, and CF$_3$CO$_2^-$) and then energy-minimized using the Amsterdam Density Functional (ADF) 2004.01 software package.[40−42] A model of [Fe^{IV}(O)(TMCS)]$^+$

(31) Armarego, W. L. F.; Perrin, D. D. *Purification of Laboratory Chemicals*; Butterworth-Heinemann: Oxford, U.K., 1997.
(32) Saltzman, H.; Sharefkin, J. G. *Organic Syntheses*; Wiley: New York, 1973; Vol. V.

(33) Scarrow, R. C.; Maroney, M. J.; Palmer, S. M.; Roe, A. L.; Que, L., Jr.; Salowe, S. P.; Stubbe, J. *J. Am. Chem. Soc.* **1987**, *109*, 7857–7864.
(34) Shu, L.; Chiou, Y.-M.; Orville, A. M.; Miller, M. A.; Lipscomb, J. D.; Que, L., Jr. *Biochemistry* **1995**, *34*, 6649–6659.
(35) Rohde, J.-U.; Torelli, S.; Shan, X.; Lim, M. H.; Klinker, E. J.; Kaizer, J.; Chen, K.; Nam, W.; Que, L., Jr. *J. Am. Chem. Soc.* **2004**, *126*, 16750–16761.
(36) George, G. N. *EXAFSPAK*; Stanford Synchrotron Radiation Laboratory: Stanford, CA, 1990.
(37) Klinker, E. J.; Jackson, T. A.; Jensen, M. P.; Juhasz, G.; Münck, E.; Que, L., Jr. *Angew. Chem., Int. Ed* **2006**, *45*, 7394–7397.
(38) Scarrow, R. C.; Trimitsis, M. G.; Buck, C. P.; Grove, G. N.; Cowling, R. A.; Nelson, M. J. *Biochemistry* **1994**, *33*, 15023–15035.
(39) Pestovsky, O.; Stoian, S.; Bominaar, E. L.; Shan, X.; Münck, E.; Que, L., Jr.; Bakac, A. *Angew. Chem., Int. Ed* **2005**, *44*, 6871–6874.
(40) te Velde, G.; Baerends, E. J. *J. Comput. Phys.* **1992**, *99*, 84–98.
(41) Guerra, C. F.; Snijders, J. G.; te Velde, G.; Baerends, E. J. *Theor. Chem. Acc.* **1998**, *99*, 391–403.

was likewise generated using the previously optimized geometry[30] as a starting point for DFT energy minimization. These computations were carried out on a cluster consisting of Intel Xeon processors (Ace Computers) using uncontracted triple-ζ Slater-type orbitals including a single set of polarization functions as a basis set (ADF basis set IV), an integration constant of 4.0, and the local density approximation of Vosko et al.[43] with the nonlocal gradient corrections of Becke[44] and Perdew.[45] Core orbitals were frozen through 1s (O, N, C) and 2p (Fe and S). Calculations were converged to the $S = 1$ spin state. The coordinates of all DFT energy-minimized models presented in this study are included as Supporting Information (Tables S4–S11).

2.3.2. Calculation of Excited-State Properties. Electronic transition energies were computed using both the ADF 2004.01 and ORCA 2.5 software packages, the latter of which was developed by Dr. Frank Neese (University of Bonn, Germany).[46] Using the ADF program, we computed the electronic transition energies by the so-called ΔSCF method[2,47−49] where an electron is excited from the donor to the acceptor molecular orbital (MO) and the change in total energy at convergence is taken as the electronic transition energy. Excited-state geometry optimizations were performed using the excited-state density as a starting point for energy minimization of the nuclear coordinates. MO compositions were inspected before and after these computations to determine if the ΔSCF procedure had maintained the electronic structure of the excited state and not reverted back to the ground state. In all cases, the excited-state MO compositions were virtually identical (changes in contribution of ~2% were observed) before and after energy minimization of the nuclear coordinates.

The ORCA program was used to compute electronic excitation energies and intensities for **1**-NCMe, **1**-N$_3$, **1**-NCS, and **1**-NCO using the time-dependent (TD)-DFT[50−52] method within the Tamm−Dancoff approximation.[53,54] To determine which functional yields computed absorption spectra in closest agreement with our experimental data, we computed absorption spectra for **1**-NCMe using the BP86,[44,45] B3LYP,[55−57] and PBE0[58] functionals. For these computations, the SV(P) (Ahlrichs polarized split valence) basis[59] was used for all H atoms and the C atoms of the TMC macrocycle, whereas the TZVP (Ahlrichs polarized triple-ζ valence) basis[59] was used for Fe, O, N, and S, as well as the C atoms of the axial ligands. The size of the integration grid used for all calculations was 3 (Lebedev 194 points). In each case, 40 excited
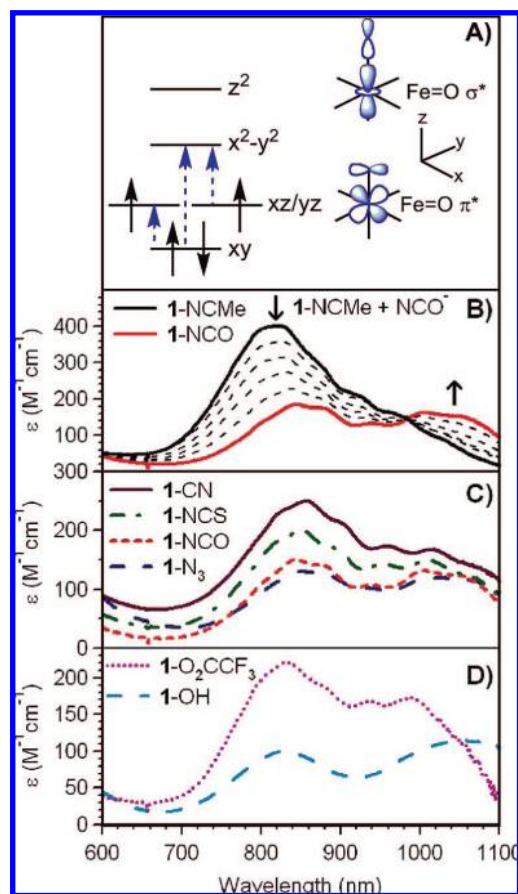
(42) *ADF2004.01*; Vrije Universiteit: Amsterdam, The Netherlands, 2004; http://www.scm.com.
(43) Vosko, S. H.; Wilk, L.; Nusair, M. *Can. J. Phys.* **1980**, *58*, 1200–1211.
(44) Becke, A. D. *J. Chem. Phys.* **1986**, *84*, 4524–4529.
(45) Perdew, J. P. *Phys. Rev. B* **1986**, *33*, 8822–8824.
(46) Neese, F. *ORCA - An ab Initio, Density Functional and Semiempirical Program Package*, version 2.5; University of Bonn: Bonn, Germany, 2006.
(47) Brunold, T.; Herren, M.; Oetliker, U.; Güdel, H. U.; Kesper, U.; Albrecht, C.; Reinen, D. *J. Lumin.* **1994**, *60–61*, 138–141.
(48) Brunold, T. C.; Tamura, N.; Kitajima, N.; Moro-oka, Y.; Solomon, E. I. *J. Am. Chem. Soc.* **1998**, *120*, 5674–5690.
(49) Brunold, T. C.; Gamelin, D. R.; Stemmler, T. L.; Mandal, S. K.; Armstrong, W. H.; Penner-Hahn, J. E.; Solomon, E. I. *J. Am. Chem. Soc.* **1998**, *120*, 8724–8738.
(50) Bauernschmitt, R.; Ahlrichs, R. *Chem. Phys. Lett.* **1996**, *256*, 454–464.
(51) Casida, E. M.; Jamorski, C.; Casida, K. C.; Salahub, D. R. *J. Chem. Phys.* **1998**, *108*, 4439–4449.
(52) Stratman, R. E.; Scuseria, G. E.; Frisch, M. J. *J. Chem. Phys.* **1998**, *109*, 8218–8224.
(53) Hirata, S.; Head-Gordon, M. *Chem. Phys. Lett.* **1999**, *302*, 375–382.
(54) Hirata, S.; Head-Gordon, M. *Chem. Phys. Lett.* **1999**, *314*, 291–299.
(55) Becke, A. D. *J. Chem. Phys.* **1993**, *98*, 5648–5652.
(56) Becke, A. D. *J. Chem. Phys.* **1993**, *98*, 1372–1377.
(57) Lee, C.; Yang, W.; Parr, R. G. *Phys. Rev. B* **1988**, *37*, 785–789.
(58) Perdew, J. P.; Burke, K.; Ernzerhof, M. *Phys. Rev. Lett.* **1996**, *77*, 3865–3868.
(59) Schäfer, A.; Horn, H.; Ahlrichs, R. *J. Chem. Phys.* **1992**, *97*, 2571–2577.

Figure 2. NIR regions of the electronic absorption spectra of [Fe^{IV}(O)(T-MC)(X)]$^{2+/+}$ complexes in MeCN at −40 °C. (A) General Fe^{IV} 3d orbital splitting diagram for nonheme oxoiron(IV) complexes, with the three NIR d−d transitions identified through MCD studies (ref 62) indicated with dashed arrows. (B) NIR spectrum of 4 mM [Fe^{IV}(O)(TMC)(NCMe)]$^{2+}$ (**1**-NCMe) and spectral changes following the addition of 10 equiv of NBu$_4$NCO. (C) Spectra of 4 mM [Fe^{IV}(O)(TMC)(CN)]$^+$ (**1**-CN), [Fe^{IV}(O)(T-MC)(NCS)]$^+$ (**1**-NCS), [Fe^{IV}(O)(TMC)(NCO)]$^+$ (**1**-NCO), and [Fe^{IV}(O)(TMC)(N$_3$)]$^+$ (**1**-N$_3$). (D) Spectra of 2 mM [Fe^{IV}(O)(TMC)(O$_2$CCF$_3$)]$^+$ (**1**-O$_2$CCF$_3$) and 8 mM [Fe^{IV}(O)(TMC)(OH)]$^+$ (**1**-OH).

states were calculated by including all one-electron excitations within an energy window of ±3 hartrees with respect to the HOMO/LUMO energies. Isosurface plots of MOs were generated with the gOpenMol program developed by Laaksonen and co-workers[60,61] using the isodensity value of 0.05 b$^{−3}$.

3. Results and Discussion

3.1. Ligand Substitution Reactions of [Fe^{IV}(O)(TMC)(NC-Me)]$^{2+}$. The oxoiron(IV) complex [Fe^{IV}(O)(TMC)(NCMe)]$^{2+}$ (**1**-NCMe) can be generated quantitatively by the addition of an equivalent of iodosobenzene to a solution of [Fe^{II}(TM-C)(OTf)]$^+$ in MeCN, as previously reported.[18] This complex exhibits a characteristic electronic absorption feature at 824 nm ($\varepsilon = 400$ M$^{−1}$ cm$^{−1}$; Figure 2B) that arises from ligand-field (LF) transitions of the $S = 1$ Fe^{IV}=O unit (see Figure 2A for the d orbital splitting pattern).[62,63] The addition of a variety of

(60) Laaksonen, L. *J. Mol. Graphics* **1992**, *10*, 33–34.
(61) Bergman, D. L.; Laaksonen, L.; Laaksonen, A. *J. Mol. Graphics Model.* **1997**, *15*, 301–306.
(62) Decker, A.; Rohde, J.-U.; Que, L., Jr.; Solomon, E. I. *J. Am. Chem. Soc.* **2004**, *126*, 5378–5379.
(63) Decker, A.; Rohde, J.-U.; Klinker, E. J.; Wong, S. D.; Que, L., Jr.; Solomon, E. I. *J. Am. Chem. Soc.* **2007**, *129*, 15983–15996.

Table 1. Physical Properties of $[Fe^{IV}(O)(TMC)(X)]^{2+/+}$ (**1-X**) Complexes[a]

	λ_{max} (nm) (ε (M^{-1}cm^{-1}))	$t_{1/2}$ at 25 °C[b]	ν_{FeO} (cm^{-1})	δ (mm/s)	ΔE_Q (mm/s)	η	D (cm^{-1})[c]	$A_x/g_n\beta_n$ (T)[d]	$A_y/g_n\beta_n$ (T)[d]	$A_z/g_n\beta_n$ (T)[d]
1-NCMe	282 (10 000) 824 (400)	10 h[e]	839 (804)	0.17[f]	1.23[f]	0.5[f]	29[f]	−23[f]	−18[f]	−3[f]
1-O₂CCF₃	836 (250)	1 h[e]	854 (817)	0.20	1.39	0	31	−24	−22	−3
1-NCO	350 (3100) 845 (150) 1010 (130)	30 min	822 (792)	0.16	0.42	0.1	31	−23	−23	−5
1-NCS	387 (3500) 850 (200) 1010 (170)	30 min	820 (786)	0.16	0.60	0.2	30	−24	−20	−4
1-N₃	407 (3600) 850 (130) 1050 (110)	15 min	814 (780)	0.17	0.70	0.1	29	−24	−20	−5
1′-SR	460 (1300) 570 (1100) 860 (230)	5 min	ND[g]	0.19[h]	−0.22[h]	0[h]	35[h]	−23[h]	−22[h]	−5[h]
1-CN	858 (250)	1.5 h	823 (789)	0.15	0.25	0.9	31	−21	−20	−5
1-OH	830 (100) 1060 (110)	~seconds	ND[g]	0.15	0.16	−3.0	31	−22	−22	−2

[a] Estimated uncertainties for Mössbauer parameters are as follows. δ: ±0.01 mm/s, ΔE_Q: ±0.05 mm/s, D: 2 cm^{-1}, $A_i/g_n\beta_n$: 2.5 T. [b] Half-lives were determined by monitoring the decay of 4 mM $[Fe^{IV}(O)(TMC)(X)]^+$ using UV−visible spectroscopy at 25 °C. [c] The Mössbauer spectra of the **1-X** complexes are sensitive to the internal magnetic field at the ^{57}Fe nucleus, $\mathbf{B}_{int} = -\langle S\rangle_{th}\bullet\mathbf{A}/g_n\beta_n$, where $\langle S\rangle_{th}$ is the thermal expectation value of the electronic spin. The value of $\langle S\rangle_{th}$ depends on D, E, $\mathbf{B}$, and the temperature. In our simulations, we found no need to use $E/D > 0$. Simulations with $E/D > 0$ would require larger A_x and smaller A_y values, keeping the magnetic hyperfine field axial around z. [d] The D values of all **1-X** complexes are very large, and consequently the components of the magnetic hyperfine field are essentially proportional to g_iA_i ($i = x$, y, z). Thus, any increase of the g_i values above the assumed values of $g_i = 2.0$ would yield a decrease in the component A_i. [e] Reference 26. [f] Reference 18. [g] Not determined. Despite several attempts, to date, we have not observed ν_{FeO} for **1′-SR** and **1-OH**. [h] Reference 30.

tetralkylammonium salts (NR₄X; where X = OH⁻ and the pseudohalides N₃⁻, NCS⁻, NCO⁻, and CN⁻) to **1**-NCMe (eq 1) causes a loss of NIR intensity and a shift of the NIR λ_{max} (Figure 2 and Table 1). In all cases, isosbestic behavior is observed (see Figure 2B for X = NCO⁻), indicating a one-step transition from **1**-NCMe to a second species we designate as **1**-X, where X is the added anion. These spectral changes are reminiscent of those observed when NBu₄O₂CCF₃ was added to **1**-NCMe.[26] In that case, ^{19}F NMR data supported the conclusion that the CF₃CO₂⁻ anion displaced the MeCN ligand to generate $[Fe^{IV}(O)(TMC)(O_2CCF_3)]^+$ (**1**-O₂CCF₃). ESI-MS data obtained for solutions of **1**-X (Figure S4) likewise allow us to formulate these species as $[Fe^{IV}(O)(TMC)(X)]^+$ (X = OH⁻, N₃⁻, NCS⁻, NCO⁻, and CN⁻), where the X anion has replaced the MeCN ligand. We previously showed that the complexes **1**-N₃ and **1**-NCS could be generated via the addition of iodosobenzene to MeCN solutions of $[Fe^{II}(TMC)(N_3)]^+$ and $[Fe^{II}(TMC)(NCS)]^+$,[28] so these current findings demonstrate that there are two general routes to these oxoiron(IV) complexes, identical to that observed for **1**-O₂CCF₃.[26]

$[Fe^{IV}(O)(TMC)(NCMe)](OTf)_2 +$

$NBu_4X \rightarrow [Fe^{IV}(O)(TMC)(X)](OTf) + NBu_4OTf + NCMe$ (1)
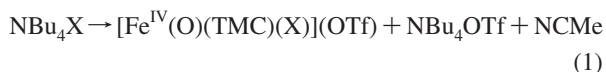
The parent oxoiron(IV) complex **1**-NCMe is remarkably stable, with a half-life of 10 h at room temperature.[26] The substitutions of MeCN with an anion in the reactions reported here all greatly diminish the thermal stability of the oxoiron(IV) center (Table 1). The series of **1**-X complexes themselves exhibit a range of thermal stabilities; at room temperature the lifetimes can be placed in decreasing order as follows: **1**-CN > **1**-O₂CCF₃ > **1**-NCS ≈ **1**-NCO > **1**-N₃ > **1**-OH. Thus, for the TMC system, negatively charged ligands do not stabilize the high-valent Fe^{IV} oxidation state and, in fact, appear to promote its decay. This is an emerging theme for nonheme oxoiron(IV) complexes, as the thermal decay of the related $[Fe^{IV}(O)(T-PA)(NCMe)]^{2+}$ complex (Figure 1B) is also hastened by

replacing the MeCN ligand with the anions CF₃CO₂⁻, Cl⁻, and Br⁻.[25] The MeCN ligand would therefore appear to stabilize the Fe^{IV}=O unit.

3.2. Spectroscopic Data. 3.2.1. Near-Infrared Absorption Data. Relative to that of **1**-NCMe, the NIR λ_{max} values of the **1**-X complexes red-shift from 824 nm to ∼830−850 nm and exhibit a more than 2-fold loss of absorption intensity (Figure 2 and Table 1). On the basis of detailed magnetic circular dichroism (MCD) studies of **1**-NCMe and **1**-O₂CCF₃,[62,63] these spectral perturbations are attributed to π-interactions between the Fe^{IV} d$_{xz/yz}$ and X p$_{x/y}$ orbitals, which modulate the energies and intensities of the d$_{xy} \rightarrow$ d$_{xz/yz}$ and d$_{xz/yz} \rightarrow$ d$_{x^2-y^2}$ transitions (Figure 2A). Because the Fe^{IV} d$_{xz/yz}$ orbitals are Fe=O π-antibonding,[63,64] these NIR spectral changes thus mark perturbations in Fe=O π-interactions caused by the trans ligand.

It is notable that several of the **1**-X complexes (i.e., those with X = NCS⁻, NCO⁻, and CN⁻) exhibit sharper features on top of their broader absorption envelopes. For example, **1**-NCS displays λ_{max} values at 850, 892, 953, and 1010 nm. In principle, these sharp features could be due to spin-forbidden Fe^{IV} d → d transitions that are expected to be much sharper than their spin-allowed counterparts. However, given that the low-temperature MCD spectra of **1**-NCMe and **1**-O₂CCF₃ displayed fine structure that was assigned as vibronic in origin,[62,63] we likewise attribute the fine structure observed in the absorption spectra of certain **1**-X complexes to a vibronic progression that is better resolved for these complexes. In fact, because MCD studies showed that the d$_{xy} \rightarrow$ d$_{xz/yz}$ transitions of **1**-NCMe exhibit well-resolved vibronic structures, this band must gain significant absorption intensity in some of the **1**-X complexes, further reflecting electronic perturbations due to the trans ligand.

3.2.2. Visible and Near-UV Absorption Data. In addition to the NIR spectral changes, the **1**-N₃, **1**-NCS, and **1**-NCO complexes also exhibit clear absorption bands in the visible/near-UV spectral region (Figure 3 and Table 1), the intensities

(64) Decker, A.; Clay, M. D.; Solomon, E. I. *J. Inorg. Biochem.* **2006**, *100*, 697–706.
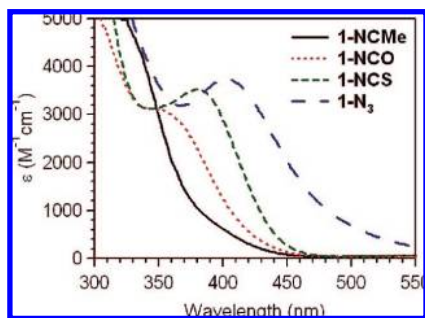
Figure 3. Expanded view of the visible/near-UV region of the electronic absorption spectra of $[Fe^{IV}(O)(TMC)(NCMe)]^{2+}$ (**1**-NCMe), $[Fe^{IV}(O)(TMC)(NCO)]^{+}$ (**1**-NCO), $[Fe^{IV}(O)(TMC)(NCS)]^{+}$ (**1**-NCS), and $[Fe^{IV}(O)(TMC)(N_3)]^{+}$ (**1**-N$_3$) obtained at −40 °C in MeCN.

of which ($\varepsilon \approx 3000$ M^{-1} cm^{-1}) are consistent with charge-transfer (CT) transitions. This is in contrast to the corresponding spectrum collected for **1**-NCMe that only shows the onset of absorption intensity at ∼350 nm (Figure 3) and an absorption maximum at 282 nm.[28] The **1**-N$_3$, **1**-NCS, and **1**-NCO complexes likewise show additional intense features further into the UV region, though the onset of these features is blue-shifted relative to **1**-NCMe for **1**-NCS and **1**-NCO (Figure 3). The visible absorption bands of **1**-N$_3$ and **1**-NCS were previously reported and tentatively assigned as $O^{2-} \rightarrow Fe^{IV}$ CT transitions, because resonance Raman experiments using a 407-nm excitation wavelength permitted the observation of the Fe=O stretching vibration (ν_{FeO}), whereas no pseudohalide-related vibrations were observed.[28] Because **1**-NCMe does not display significant absorption intensity at wavelengths greater than ∼350 nm, this assignment requires that the binding of the N$_3^-$ and NCS$^-$ ligands causes a red-shift in the energy of the $O^{2-} \rightarrow Fe^{IV}$ CT transitions. This in turn suggests a large modulation of the Fe=O bonding interactions in these complexes. To date, the only other examples of oxoiron(IV) complexes that exhibit relatively low-energy charge-transfer transitions are **1**-NCO (Figure 3) and **1′**-SR.[30] The absorption spectrum for **1′**-SR displays two prominent absorption features in the visible region at 460 and 570 nm (Table 1).[30] This complex also displays a longer Fe=O bond length of 1.70 Å, demonstrating the large effect of the thiolate ligand on the geometric properties of the Fe=O unit. Consequently, the geometric structures, particularly the Fe=O distances of the **1**-X complexes, are of significant interest. But efforts to crystallize the other **1**-X complexes have thus far been unsuccessful, so we turned to X-ray absorption spectroscopy to obtain metric parameters for these relatively unstable complexes.

3.2.3. X-ray Absorption Data. X-ray Absorption Near-Edge Structures. XAS data at the Fe K-edge were measured for **1**-NCMe and several **1**-X complexes (X = CF$_3$CO$_2^-$, N$_3^-$, NCS$^-$, NCO$^-$, CN$^-$, and OH$^-$). The X-ray absorption near-edge structures (XANES) of the **1**-X complexes are shown in Figures 4 and S4 and summarized in Table 2. The Fe K-edge energies of all complexes are at ∼7125 eV, consistent with values previously reported for oxoiron(IV) species[25,30,35] and similar to that recently reported for a nonheme oxoiron(V) complex of a tetraamido macrocyclic ligand (7125.3 eV).[65] The range of edge energies observed for this present series of complexes could be due to different degrees of electron
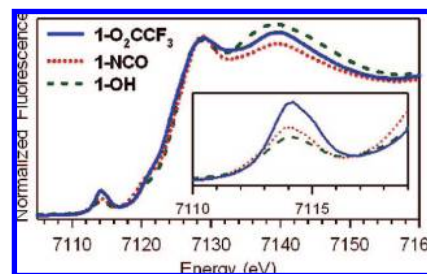
(65) Tiago de Oliveira, F.; Chanda, A.; Banerjee, D.; Shan, X.; Mondal, S.; Que, L., Jr.; Bominaar, E. L.; Münck, E.; Collins, T. J. *Science* **2007**, *315*, 835–838.

Figure 4. Fe K-edge XANES of $[Fe^{IV}(O)(TMC)(O_2CCF_3)]^{+}$ (**1**-O$_2$CCF$_3$), $[Fe^{IV}(O)(TMC)(NCO)]^{+}$ (**1**-NCO), and $[Fe^{IV}(O)(TMC)(OH)]^{+}$ (**1**-OH) obtained at 10 K.

Table 2. Fe K-Edge XAS Near-Edge Properties of $[Fe^{IV}(O)(TMC)(X)]^{2+/+}$ (**1**-X) Complexes

	E_0 (eV)	$E_{pre-edge}$ (eV)	area	weighted area[a]	%Fe^{IV} [b]	contaminants[c]
1-NCMe	7124.5	7114.1	26.2	32.8	80	20% Fe^{II}
1-O$_2$CCF$_3$	7124.0	7114.2	30.9	38.6	80	20% Fe^{III}
1-NCO	7125.3	7114.7	25.9	30.5	85	11% Fe^{II}
1-NCS	7125.4	7114.3	23.9	29.1	*82*	18% Fe^{III}
1-N$_3$	7125.3	7114.4	24.3	29.6	*82*	18% Fe^{III}
1′-SR[d]	7125.1	7114.3	18.0	20.0	90	8% Fe^{II}
1-CN	7124.8	7114.1	21.0	26.2	80	10% Fe^{II} + 12% Fe^{III}
1-OH	7125.4	7115.1	19.5	21.7	*90*	10% Fe^{II}

[a] Area weighted by percentage Fe^{IV} in the samples. The presence of contaminants introduces a maximum error in pre-edge areas of ±2 units. [b] Percentage Fe^{IV} determined by Mössbauer or absorption (italics) spectroscopy. [c] All contaminants are high-spin Fe^{II} or Fe^{III} as determined by Mössbauer spectroscopy. [d] From ref 30.

donation to the Fe^{IV} center by the different X ligands. Alternatively, differing amounts of unreacted Fe^{II} starting material and Fe^{III}/Fe^{II} decay products present in the samples, as detected by Mössbauer experiments, could also lead to slight downshifts in the edge energies. These contaminants are also listed in Table 2.

All complexes exhibit one prominent pre-edge transition at ∼7114.5 ± 0.6 eV, the area of which is strongly dependent on the identity of the X ligand (Figure 4 and Table 2). In this study, **1**-O$_2$CCF$_3$ and **1**-OH represent the extremes, having pre-edge areas of ∼39 and ∼22 units, respectively (Table 2). These pre-edge features arise from parity-forbidden Fe 1s → 3d transitions that gain intensity through Fe 4p and 3d mixing allowed by low symmetry distortions.[66] Oxoiron(IV) complexes have severe axial distortions due to their short Fe=O bond lengths of ∼1.65 Å[18,21,25,30,35] and thus generally exhibit large pre-edge areas of ∼25 units.[25,35] We note that the basicity of the trans ligand, likely marking its donor strength, appears to correlate with the pre-edge area, as complexes with more basic trans ligands (i.e., OH$^-$ and RS$^-$) have the lowest pre-edge areas (∼20−22), while the **1**-O$_2$CCF$_3$ complex with the least basic CF$_3$CO$_2^-$ ligand exhibits the highest pre-edge area of ∼39 units (Table 2). The latter value is comparable to those observed for oxoiron(IV) porphyrin and tetraamido macrocyclic ligand complexes (∼35−41 units).[67,68]

(66) Westre, T. E.; Kennepohl, P.; DeWitt, J. G.; Hedman, B.; Hodgson, K. O.; Solomon, E. I. *J. Am. Chem. Soc.* **1997**, *119*, 6297–6314.

(67) (a) Nam, W.; Choi, S. K.; Lim, M. H.; Rohde, J.-U.; Kim, I.; Kim, J.; Kim, C.; Que, L., Jr. *Angew. Chem., Int. Ed.* **2003**, *42*, 109–111. (b) Wolter, T.; Meyer-Klaucke, W.; Müther, M.; Mandon, D.; Winkler, H.; Trautwein, A. X.; Weiss, R. *J. Inorg. Biochem.* **2000**, *78*, 117–122.

(68) Chanda, A.; Shan, X.; Chakrabarti, M.; Ellis, W. C.; Popescu, D. L.; Tiago de Oliveira, F.; Wang, D.; Que, L., Jr.; Collins, T. J.; Münck, E.; Bominaar, E. L. *Inorg. Chem.* **2008**, *47*, 3669–3678.
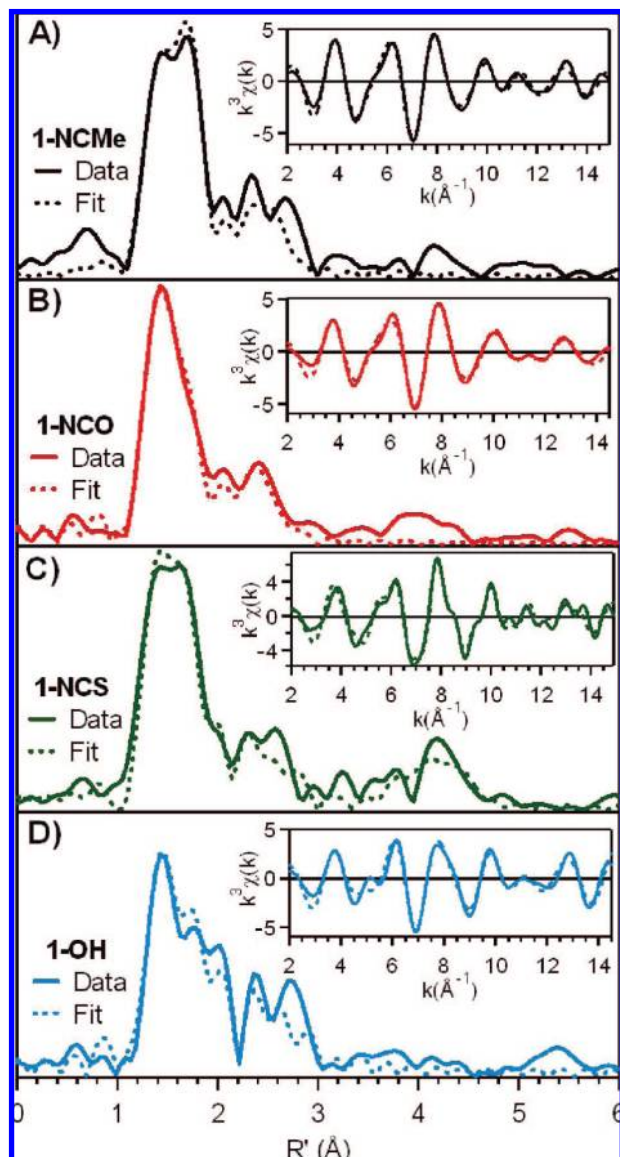
Figure 5. Fourier transforms of Fe K-edge EXAFS data [$k^3\chi(k)$] and Fourier-filtered EXAFS spectra (insets), experimental data (—) and fits (···) for (A) [Fe^{IV}(O)(TMC)(NCMe)]$^{2+}$ (**1**-NCMe), (B) [Fe^{IV}(O)(TMC)(NCO)]$^+$ (**1**-NCO), (C) [Fe^{IV}(O)(TMC)(NCS)]$^+$ (**1**-NCS), and (D) [Fe^{IV}(O)(TM-C)(OH)]$^+$ (**1**-OH). Details regarding the EXAFS fits are given in Tables 3, S1, and S2.

3.2.3.1. EXAFS Data and Fitting Results for 1-NCMe. The Fourier transform (R' space) of the Fe K-edge EXAFS data of **1**-NCMe in frozen MeCN solution exhibits several prominent peaks that can be best accounted for by three shells at 1.64 (one O scatterer), 2.08 (five N scatterers), and 2.97 Å (four C scatterers), as shown in Figure 5A and Table 3. The distances of the inner shells of O and N scatterers are in good agreement with the Fe—O and average Fe—N distances of 1.646 and 2.084 Å observed in the X-ray structure of **1**-NCMe.[18] The X-ray structure also reveals 10 C atoms ~2.8–3.1 Å from the Fe center, which likely contribute to the R' space peaks at 2.4 and 2.7 Å. The relatively large discrepancy in number of C scatterers required to fit these peaks (four C scatterers) is attributed to the distribution of Fe—C distances, leading to some destructive interference among the various contributions. Overall, the EXAFS fitting results are in excellent agreement with the crystallographic data, especially in terms of the iron—ligand

distances. Thus, the EXAFS technique is well suited to determine if there is any large structural variation within the **1**-X series of complexes that could account for differences in spectroscopic properties and/or thermal stabilities.

3.2.3.2. EXAFS Data and Fitting Results for 1-X Complexes. The R' space spectra for the **1**-X complexes are quite similar to that of **1**-NCMe (Figures 5 and S6). There is a moderate degree of variation in the peak centered at ~1.6 Å that arises from the first-coordination sphere, whereas the peaks from ~2 to 3 Å are nearly invariant of ligand substitution. Consequently, similar iron-scatterer distances were obtained from fitting these data sets, as summarized in Table 3. Two special cases are **1**-OH and **1**-NCS.

For **1**-OH, the FT peak from the inner shell is quite distinct from that of **1**-NCMe (cf. Figure 5A,D). Accordingly, the EXAFS data for **1**-OH are best fit with a longer Fe—O distance of 1.68 Å and an additional Fe—O shell at 1.94 Å, the latter of which we attribute to the O atom of the hydroxo ligand. This distance is significantly longer than the Fe^{IV}—OH distances observed for compound II of chloroperoxidase[69] and [Fe^{IV}(BP-MCN)(OH)(OO'Bu)]$^{2+}$ (where BPMCN is *N,N'*-bis(2-pyridyl-methyl)-*N,N'*-dimethyl-*trans*-1,2-diaminocyclohexane),[70] which are both 1.82 Å. It is also slightly longer than the Fe^{IV}—OH distance of 1.86 Å computed for a model of the oxoiron(IV) intermediate of the His99Ala variant of TauD, where the H99A substitution opens a coordination site for OH$^-$ that is cis to the oxo ligand.[71] On the basis of these observations, we attribute the longer Fe^{IV}—OH distance of **1**-OH to the distinct influences of the *trans*-oxo ligand that modulates the binding affinity of the iron(IV) center for the hydroxide ligand. This is consistent with computations by Berry et al. that predicted an elongation of an Fe—O(acetate) distance by 0.15 Å upon going from a *trans*-fluoro to an oxo ligand.[72]

For **1**-NCS, the R' space spectrum from ~1 to 2.8 Å appears virtually the same as that of **1**-NCMe, indicating that the NCS$^-$ ligand is not S-bound, as that would lead to relatively large spectral changes in this region. In contrast, the FT spectrum of **1**-NCS displays a peak at $R' = 4.2$ Å that is almost as intense as the peak attributed to the C shell at ~2.5 Å (Figure 5C). An intense peak at such a relatively long distance from the Fe center is anticipated only for a heavy-atom scatterer, the S atom of the NCS ligand being the obvious candidate. In support, the inclusion of four prominent multiple-scattering paths associated with a linear Fe—NCS unit led to quite reasonable fits (Table 3). Thus, these EXAFS data provide strong evidence that the NCS ligand coordinates through the N atom in a linear fashion, in agreement with the linear, N-bound NCS ion observed in the crystal structure of [Fe^{II}(TMC)(NCS)]$^+$.[28]

Intriguingly, the FT EXAFS data for **1**-NCMe and **1**-NCO also display peaks at ~4.2 Å, albeit ones less intense than that observed for **1**-NCS (cf. Figure 5A–C). We suggest that these peaks also have their origin in multiple-scattering effects that are amplified because of linear binding of the NCO$^-$ and NCMe ligands. In contrast, the absence of such a peak for **1**-N$_3$ (Figure S6) implies that the N$_3^-$ anion binds to the Fe^{IV} center with a

(69) Green, M. T.; Dawson, J. H.; Gray, H. B. *Science* **2004**, *304*, 1653–1656.
(70) Jensen, M. P.; Costas, M.; Ho, R. Y. N.; Kaizer, J.; Mairata i Payeras, A.; Münck, E.; Que, L., Jr.; Rohde, J.-U.; Stubna, A. *J. Am. Chem. Soc.* **2005**, *127*, 10512–10525.
(71) Sinnecker, S.; Svensen, N.; Barr, E. W.; Ye, S.; Bollinger, J. M., Jr.; Neese, F.; Krebs, C. *J. Am. Chem. Soc.* **2007**, *129*, 6168–6179.
(72) Berry, J. F.; Bill, E.; Bothe, E.; Neese, F.; Wieghardt, K. *J. Am. Chem. Soc.* **2006**, *128*, 13515–13528.

Table 3. EXAFS Fitting Results for [Fe^{IV}(O)(TMC)(X)]$^{2+/+}$ (**1**-X) Complexes

	Fe−O^a			Fe−N^a			Fe···C			Fe−X		
	n	r (Å)	$\sigma^2 \times 10^3$ (Å^2)	n	r (Å)	$\sigma^2 \times 10^3$ (Å^2)	n	r (Å)	$\sigma^2 \times 10^3$ (Å^2)	n	r (Å)	$\sigma^2 \times 10^3$ (Å^2)
1-NCMe	1	1.64	3.8	5	2.08	5.7	4	2.97	6.5			
1-O$_2$CCF$_3$	1	1.64	1.7	4	2.08	2.1	4	2.94	5.0			
1-NCO	1	1.67	1.7	5	2.07	7.1	5	2.94	8.1			
1-NCS	1	1.65	2.6	5	2.07	4.3	4	2.95	4.2	4^b	4.78^c	5.4
1-N$_3$	1	1.66	2.0	5	2.08	6.4	6	2.99	11.6			
1′-SR^e	1	1.70	1.0	3	2.09	2.0	4	2.95	6.3	1	2.33^c	0.6
1-CN	1	1.66	1.3	4	2.08	3.1	4	2.95	4.4			
1-OH	1	1.68	1.2	4	2.10	2.6	6	3.03	5.9	1	1.94^d	2.0

^{a} Typical uncertainties in Fe−O and Fe−N distances determined by EXAFS analysis are ±0.02 Å. ^{b} The fit includes the four most prominent multiple scattering pathways, each of which involves two of the three atoms of the NCS$^-$ ligand. ^{c} X = S. ^{d} X = O. ^{e} From ref 30.

bent orientation (i.e., the O−Fe−N(N$_2$) angle is <180°), consistent with a bent Fe^{III}−N$_3$ unit observed in the crystal structure of the related complex [Fe^{III}(N$_3$)(Me$_3$cylamacetate)]$^+$ (where Me$_3$cyclamacetate is 4,8,11-trimethyl-1,4,8,11-tetraaza-cyclotetradecane-1-acetate).[73]

Overall, our EXAFS analysis reveals that, except for **1′**-SR and **1**-OH, all Fe−O distances are 1.65 ± 0.02 Å, which is the standard error associated with absorber−scatterer distances obtained by this method.[74] Thus, despite the differences in spectroscopic properties (Figures 3 and 4), thermal stabilities (Table 1), and reactivities,[27] the majority of the **1**-X complexes have very similar Fe−O distances. We next turned to a spectroscopic technique that can, in principle, be an exquisitely sensitive reporter of bond length, resonance Raman spectroscopy.

3.2.4. Resonance Raman Data. Resonance Raman spectra were collected for **1**-NCMe and members of the **1**-X series of complexes using an excitation wavelength of 407 nm and a spinning sample maintained at a temperature between −20 and −40 °C. The RR spectrum obtained for **1**-NCMe displays a vibration at 839 cm^{-1} that shifts to 804 cm^{-1} upon the introduction of ^{18}O (Figure 6). This downshift is close to the calculated value for a diatomic Fe−O vibration (−34 cm^{-1}) and allows us to assign the 839 cm^{-1} feature to the Fe=O stretching vibration, ν_{FeO}. The corresponding vibration in the solid state was previously observed at 834 cm^{-1} using IR spectroscopy.[18] RR spectra collected for members of the **1**-X family revealed features in the range of 814−854 cm^{-1} (Table 1) that shifted to lower energy by ~33−37 cm^{-1} when either PhI^{18}O was used to prepare the samples or the samples were incubated with H$_2$^{18}O. The ν_{FeO} energies for the **1**-X complexes decrease in the order CF$_3$CO$_2$$^-$ ≫ MeCN > CN$^-$ ≈ NCO− ≈ NCS$^-$ > N$_3$$^-$, with lower ν_{FeO} values observed for complexes with stronger trans donor ligands. Unfortunately, attempts to obtain the ν_{FeO} of complexes with even more basic ligands such as axial-thiolate-ligated [Fe^{IV}(O)(TMCS)]$^+$ and **1**-OH were stymied by problems with fluorescence and photoreduction, and therefore the frequencies observed span only a relative small range of 40 cm^{-1}. With the use of a Badger's rule correlation described by Green[75] for nonheme iron centers (Supporting Information), bond length changes of only 0.02 Å are predicted when the extreme ν_{FeO} frequencies from **1**-O$_2$CCF$_3$ and **1**-N$_3$ are considered, consistent with our EXAFS analysis. Nonetheless, to date, this effort represents the only collection of ν_{FeO} frequencies for a series of nonheme oxoiron(IV) complexes.
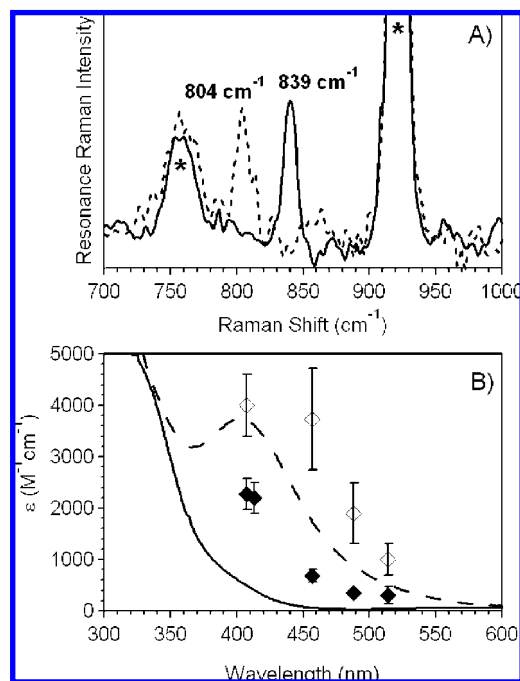

Figure 6. (A) Resonance Raman spectra of 4 mM [Fe^{IV}(O)(TMC)-(NCMe)]$^{2+}$ in MeCN prepared with PhIO (—) and with added H$_2$^{18}O (−−−) using an excitation wavelength of 407 nm. The sample was spinning during data collection and maintained at a temperature of −20 °C. Raman peaks associated with solvent vibrations are marked with an asterisk. (B) Superposition of the electronic absorption spectra and resonance Raman excitation profiles of the ν_{FeO} vibrations for [Fe^{IV}(O)(TMC)(NCMe)]$^{2+}$ (solid line, ◆) and [Fe^{IV}(O)(TMC)(N$_3$)]$^+$ (dashed line, ◇). Error bars indicate two standard deviations from three experiments.

In general, the RR data support the notion that increased basicity of the trans ligand weakens the Fe=O bond, consistent with our EXAFS data that revealed the longest Fe=O bond lengths for **1**-OH and **1′**-SR (Table 3). A similar trend was observed for the axial ligand effect on oxoiron(IV) porphyrin complexes. For example, in a resonance Raman study of five [Fe(O)(TMP$^•$)(X)]$^+$ complexes (TMP$^•$ = one-electron oxidized derivative of tetramesitylporphin dianion; X = Cl$^-$, F$^-$, *m*-chlorobenzoate, OTf$^-$, and ClO$_4$$^-$),[76] Kincaid and co-workers found the ν_{FeO} frequencies to fall into two narrow ranges, 801−806 cm^{-1} for the first three complexes and 834−835 cm^{-1} for complexes of the much weaker triflate and perchlorate ligands. Similarly, Gold et al. showed that the ν_{FeO} frequencies of [Fe^{IV}(O)(Cl$_8$TPP)(L)] (Cl$_8$TPP = tetrakis(2,6-dichlorophenyl)porphin dianion; L = THF, DMF, 1-methylimidazole)

(73) Berry, J. F.; Bill, E.; Bothe, E.; Weyhermüller, T.; Wieghardt, K. *J. Am. Chem. Soc.* **2005**, *127*, 11550−11551.
(74) Scott, R. A. In *Physical Methods in Bioinorganic Chemistry: Spectroscopy and Magnetism*; Que, L., Jr., Ed.; University Science Books: Sausalito, CA, 2000; pp 465−503.
(75) Green, M. T. *J. Am. Chem. Soc.* **2006**, *128*, 1902−1906.

(76) Czarnecki, K.; Nimri, S.; Gross, Z.; Proniewicz, L. M.; Kincaid, J. R. *J. Am. Chem. Soc.* **1996**, *118*, 2929−2935.
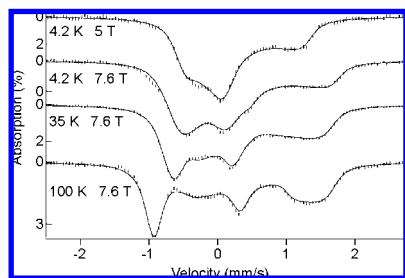
Figure 7. Mössbauer spectra of [Fe^{IV}(O)(TMC)(N$_3$)]$^+$ recorded at temperatures and applied parallel fields as indicated. Solid lines are spectral simulations based on eqs 2a and 2b using the parameters listed in Table 1. The sample contained a 20% high-spin ferric contaminant. Its 4.2 K spectral features were simulated (Figure S1) and removed from the data.

decreased from 841 to 818 cm^{-1} as the axial ligand became more electron donating.[77]

The use of RR spectroscopy to observe ν_{FeO} was previously reported for **1**-N$_3$ and **1**-NCS, for which ^{16}O/^{18}O-sensitive Raman bands were detected at 812 and 820 cm^{-1}, respectively.[28] These complexes, however, display prominent absorption bands that have maxima near the 407-nm excitation wavelength used in the RR experiment ($\lambda_{max} = 407$ and 387 for **1**-N$_3$ and **1**-NCS, respectively; Figure 3). This led us to assign those bands as O^{2-} → Fe^{IV} CT transitions.[28] The fact that similar experiments using the same excitation wavelength also allow us to observe ν_{FeO} for **1**-NCMe and other members of the **1**-X series (Table 1), most of which do not display significant absorption intensity at ∼407 nm, suggests that excitation in near resonance with an O^{2-} → Fe^{IV} CT transition that occurs with a $\lambda_{max} < 400$ nm permits the observation of ν_{FeO} as well. Support for this notion comes from an excitation profile performed for **1**-NCMe. For these experiments, the intensity of the Raman band at 839 cm^{-1} was monitored as a function of the excitation wavelength. As shown in Figure 6B, the Raman band becomes more intense as the excitation wavelength approaches the onset of absorption intensity at ∼350 nm, suggesting that this absorption feature has some contribution from an O^{2-} → Fe^{IV} CT transition. In contrast, the corresponding excitation profile for **1**-N$_3$ (Figure 6B) illustrates that the relative intensity of ν_{FeO} is increased when the excitation wavelength is in resonance with the near-UV band at 407 nm.

3.2.5. Mössbauer Data. Zero-field Mössbauer spectra were obtained for all members of the **1**-X series, and key parameters obtained from these data sets are shown in Table 1. Corresponding parameters for **1**-NCMe, **1**-N$_3$, **1**-NCS, and **1′**-SR were previously reported[18,28,30] and are shown for comparison. As can be seen from inspection of Table 1, there is a very minor variation in the isomer shift value (δ), but a rather large change in the quadrupole splitting (ΔE_Q) among the **1**-X series. The isomer shift largely marks the electron density at the Fe center and is indicative of the iron oxidation state and spin state. As such, the relatively small range of isomer shift values shown in Table 1 is consistent with the formulation of all **1**-X complexes as $S = 1$ Fe^{IV} compounds. In contrast, the quadrupole splittings span a range of nearly 1.7 mm/s, the values decreasing with increasing basicity of the axial ligand.

Additional Mössbauer data for the **1**-X complexes were collected over the temperature range from 4.2 to 120 K in parallel applied magnetic fields up to 8.0 T. These data were fit

using the spin Hamiltonian of eq 2a, where D and E are the axial and rhombic zero-field splitting (ZFS) parameters, respectively, and **A** is the magnetic hyperfine tensor. The quadrupole interactions (H_Q) depend on the principal components of the electric field gradient (EFG) tensor (**V**) and are described by V_{zz} and the asymmetry parameter of the EFG $\eta = (V_{xx} - V_{yy})/V_{zz}$. For all fits, we assumed that the ZFS, EFG, and **A** tensors are collinear and that $S = 1$ and $g = 2.0$. Although the g values of $S = 1$ Fe^{IV} complexes may deviate from 2.0, these deviations are difficult to determine by Mössbauer spectroscopy because of the large D values of these complexes. All spectra were simulated in the fast relaxation limit of the electron spin.

$$H = D(S_z^2 - 2/3) + E(S_x^2 - S_y^2) + 2\beta \mathbf{B} \cdot \mathbf{S} + \mathbf{S} \cdot \mathbf{A} \cdot \mathbf{I} + g_n\beta_n\mathrm{BoI} + H_Q \quad (2a)$$

$$H_Q = (eQV_{zz}/12)[3I_z^2 - 15/4 + \eta(I_x^2 - I_y^2)] \quad (2b)$$

Mössbauer data collected for **1**-N$_3$ at different temperatures and magnetic field strengths, along with spectral simulations using eqs 2a and 2b and the parameters listed in Table 1, are shown in Figure 7. Fits to data obtained for the other **1**-X complexes are of similar quality and yielded the corresponding parameters collected in Table 1. For all complexes, the axial ZFS parameter D is quite large (∼30 cm^{-1}), reflecting the presence of low-lying $S = 0$ and $S = 2$ excited states that mix with the $S = 1$ ground state via spin−orbit coupling.

3.3. Computations. When considered together, the spectroscopic data collected for the **1**-X series support two conclusions: (i) the Fe=O bond length is only slightly perturbed by the nature of the trans ligand (Table 3), with the hydroxide and thiolate ligands of **1**-OH and **1′**-SR, respectively, providing notable exceptions, and (ii) the electronic structure of the oxoiron(IV) unit is nonetheless modulated by the donor properties of the trans ligand, as evidenced by the dependence of the XAS preedge area and quadrupole splitting parameter on the basicity of X$^-$, and the altered electronic absorption spectra of the **1**-X complexes (Figures 2 and 3). To gain further insight into the possible origins of these experimental observations, we performed DFT computations for **1**-NCMe and all **1**-X complexes.[78]

3.3.1. DFT-Optimized Geometries. Key metric parameters of our DFT-optimized models of **1**-NCMe and all **1**-X complexes are collected in Table 4; the corresponding iron−ligand distances obtained by EXAFS analyses are shown for comparison in parentheses. The structure of **1**-NCMe is in good agreement with that determined experimentally by X-ray crystallography, except the Fe−N$_{TMC}$ distance (where Fe−N$_{TMC}$ is the average distance from the iron center to the N atoms of the TMC macrocycle) is slightly overestimated (average computed and crystallographic distances are 2.123 and 2.090 Å, respectively),[18] as was observed in previous studies by Neese and co-workers.[79,80]

(77) Gold, A.; Jayaraj, K.; Doppelt, P.; Weiss, R.; Chottard, G.; Bill, E.; Ding, X.; Trautwein, A. X. *J. Am. Chem. Soc.* **1988**, *110*, 5756−5761.

(78) DFT calculations to compute Mössbauer parameters of the **1**-X complexes were also undertaken. Our initial success in closely matching the calculated Mössbauer parameters for the parent **1**-NCMe complex with those obtained by experiment (ref 18), as well as the success of others (refs 79 and 80), led us to anticipate that the corresponding parameters of the **1**-X series could be also correctly predicted. For reasons not currently well understood, this expectation has not been borne out for **1**-X complexes independent of the basis sets or functionals used for the calculations. Since DFT-calculated ΔE_Q values typically have an error of 0.5 mm/s and most of the complexes listed in Table 1 have small ΔE_Q values, the DFT calculations yield ΔE_Q and η values that are in poor agreement with the experimental values.

(79) Neese, F. *J. Inorg. Biochem.* **2006**, *100*, 716−726.

Table 4. Iron−Ligand Bond Lengths for $[Fe^{IV}(O)(TMC)(X)]^{2+/+}$ (**1**-X) Complexes Based on DFT Computations[a]

	Fe−O (Å)	Fe−N_{TMC} (Å)	Fe−X (Å)
1-NCMe	1.646 (1.64)	2.123 (2.08)	2.087 (2.08)
1-O_2CCF_3	1.661 (1.64)	2.144 (2.08)	2.004 (2.08)
1-NCO	1.674 (1.67)	2.125 (2.07)	1.940 (2.07)
1-NCS	1.677 (1.65)	2.123 (2.07)	1.932 (2.07)
1-N_3	1.676 (1.66)	2.126 (2.08)	1.930 (2.08)
1′-SR[b]	1.697 (1.70)	2.148 (2.09)	2.342 (2.33)
1-CN	1.684 (1.66)	2.127 (2.08)	2.012 (2.08)
1-OH	1.692 (1.68)	2.108 (2.10)	1.895 (1.94)

[a] The corresponding Fe−L distances obtained by analyses of Fe K-edge EXAFS data are shown for comparison in parentheses. [b] Iron−ligand distances obtained through EXAFS analysis in ref 30.

The computed Fe−N_{TMC} distance appears, to some extent, to be a function of the size of X (Table 4). For instance, **1**-OH has computed Fe−N_{TMC} distances of ~2.11 Å, whereas **1**-O_2CCF_3 and **1′**-SR, which contain bulkier X groups, display corresponding values of >2.14 Å. For all other **1**-X complexes, the predicted distances are ~2.12 Å. This observation appears to be in contrast with the results of our EXAFS analysis that showed a nearly invariant Fe−N_{TMC} distance of ~2.08 Å (Table 3). A comparison of the predicted Fe−X distances with those obtained experimentally is somewhat problematic, as, in most cases, our EXAFS data did not require splitting the shell consisting of five nitrogen scatterers. Thus, in those cases, the Fe−X distance is either very close to the average experimental Fe−N_{TMC} distance of ~2.08 Å, or the X scatterer is effectively masked by the more intense shell. However, for **1**-OH and **1′**-SR, the Fe−OH and Fe−S distances were discernible via EXAFS analysis and are in relatively good agreement with our computed values (Table 4). Most importantly, the Fe=O bond length is the key structural parameter of interest, and this is in reasonably good agreement with our EXAFS data (Table 4).

3.3.2. Bonding Descriptions for Oxoiron(IV) Complexes. The bonding descriptions of **1**-NCMe and related species were discussed in detail elsewhere[30,62,63,79,81−83] and will be summarized here to provide a framework by which to understand perturbations due to trans substitutions. The **1**-NCMe complex has an $S = 1$ $(d_{xy})^2(d_{xz})^1(d_{yz})^1$ electron configuration, with an Fe d orbital splitting pattern best described as a deviation from octahedral splitting due to the large covalency of the oxo unit (Figure 8). The $d_{xz/yz}$ and d_{z^2} MOs are Fe=O π- and σ-antibonding, respectively, whereas the $d_{x^2-y^2}$ MO is Fe−N_{TMC} σ-antibonding. The d_{xy} MO is effectively nonbonding. The splitting of the d_{xy} and $d_{x^2-y^2}$ MOs is related to the energy difference between the triplet ($S = 1$) ground state and quintet ($S = 2$) excited state, as the lowest-energy quintet state has a $(d_{xy})^1(d_{xz})^1(d_{yz})^1(d_{x^2-y^2})^1$ configuration.

The Fe d orbital splittings of select **1**-X complexes are shown in Figure 8, and the compositions of the Fe d-based MOs involved in Fe=O bonding are collected in Table 5.[84] (For this
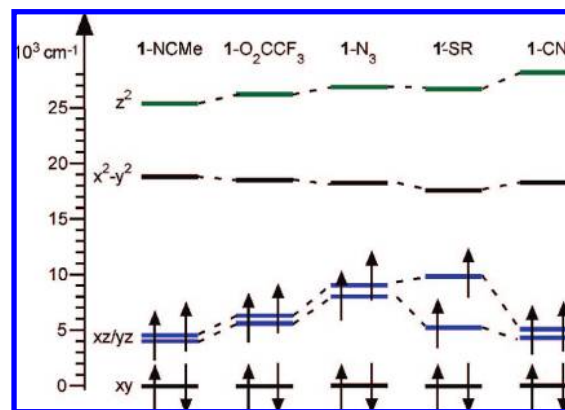
(80) Schöneboom, J. C.; Neese, F.; Thiel, W. *J. Am. Chem. Soc.* **2005**, *127*, 5840−5853.
(81) Decker, A.; Solomon, E. I. *Angew. Chem., Int. Ed.* **2005**, *44*, 2252−2255.
(82) Shaik, S.; Hirao, H.; Kumar, D. *Acc. Chem. Res.* **2007**, *40*, 532−542.
(83) Yamamoto, S.; Teraoka, J.; Kashiwagi, H. *J. Chem. Phys.* **1988**, *88*, 303−312.
(84) We performed similar computations using the pure BP86 functional, and the results are collected in Table S12. The major trends are virtually identical to those discussed for computations using the PBE0 functional, with the exception that the MO compositions are more covalent when the BP86 functional is used.

Figure 8. Molecular orbital splitting diagram for $[Fe^{IV}(O)(TMC)(X)]^{2+/+}$ (**1**-X) complexes based on DFT computations using the PBE0 hybrid functional. For comparison, the orbital energies are all plotted relative to the spin-up d_{xy} MO of each complex. MOs involved in Fe=O π- and σ-antibonding interactions are highlighted in blue and green, respectively.

Table 5. Mulliken Spin Densities and Compositions of Spin-Down Molecular Orbitals (%) Involved in Fe=O Bonding Based on PBE0 DFT Computations for Select $[Fe^{IV}(O)(TMC)(X)]^{2+/+}$ (**1**-X) Complexes

	spin density		Fe d_{xz} MO (β)			Fe d_{yz} MO (β)			Fe d_{z^2} MO (β)		
	Fe	O	Fe 3d	O 2p	X 2p	Fe 3d	O 2p	X 2p	Fe 3d	O 2p	X 2p
1-NCMe	1.36	0.81	51	36	0.9	53	34	1.1	59	19	1.1
1-O_2CCF_3	1.48	0.71	59	32	1.9	62	32	1.3	59	18	1.9
1-N_3	1.43	0.72	55	33	3.1	61	28	7.5	55	16	8.9
1′-SR	1.42	0.75	53	37	0.9	62	27	5.5	56	15	8.6
1-CN	1.37	0.82	53	36	3.9	55	35	4.1	57	15	2.6

discussion, **1**-N_3 is taken as a representative example of the pseudohalide complexes, except for **1**-CN, which is unique because of its σ-basicity and π-acidity. In addition, the bonding picture for **1**-OH is not discussed, because it has a d-orbital splitting pattern similar to that of **1′**-SR, as shown in Table S12.) Substitution of the NCMe ligand with an anion leads in all cases to destabilization of the d_{z^2} MO (Figure 8), which is greatest with the rather basic CN^- ligand. This reduces the covalency of the Fe=O σ-bond, as marked by decreased oxo p_z character in the d_{z^2} MOs for the complexes with anionic ligands. This loss is compensated by increased X^- p_z character only in the cases of **1**-N_3, and **1′**-SR, as shown in Table 5. The energies of the $d_{x^2-y^2}$ orbitals relative to the d_{xy} orbitals decrease in the order **1**-NCMe > **1**-O_2CCF_3 > **1**-CN ≈ **1**-N_3 > **1′**-SR, which follows the triplet quintet splitting computed for these complexes (excluding **1**-CN) in a separate study.[29]

Although the d_{z^2} and $d_{x^2-y^2}$ orbitals are only modestly perturbed by trans substitution, the energies and compositions of the $d_{xz/yz}$ MOs are strongly dependent on the nature of X (Figure 8 and Table 5). For **1**-O_2CCF_3, the $d_{xz/yz}$ MOs lie slightly higher in energy than those of **1**-NCMe, likely reflecting the loss of a weak Fe^{IV}−X back-bonding interaction[30] upon going from NCMe to $CF_3CO_2^-$. Consequently, the spin density is more polarized toward the Fe center for **1**-O_2CCF_3 (Table 5). Substitution of NCMe by the pseudohalide N_3^-, in contrast, leads to a pronounced destabilization (~3000−4000 cm^{-1}) of the $d_{xz/yz}$ MOs and a reduction of oxo character in the higher-energy d_{yz} MO. These changes mark a weaker Fe=O π-bond for **1**-N_3 relative to that of **1**-NCMe and **1**-O_2CCF_3, consistent with the lower ν_{FeO} observed for **1**-N_3. The weaker Fe=O π-bond for **1**-N_3 also leads to a shift of spin density toward the

Fe center, though to a lesser extent than **1**-O$_2$CCF$_3$, as some spin density is delocalized onto the pseudohalide ligand. For **1**′-SR, the orientation of the thiolate ligand is such that it has a significantly stronger π-interaction with the d$_{yz}$ than the d$_{xz}$ orbital (Table 5). Consequently, these MOs are split by ~4500 cm^{-1} (Figure 8), with the d$_{yz}$ MO at higher energy. Substitution of NCMe with the π-acidic CN$^-$ ligand maintains the Fe—X back-bonding interaction, leaving the relative energies and compositions of the d$_{xz/yz}$ MOs of **1**-CN, along with the Fe and O spin densities, virtually identical to those of **1**-NCMe (Figure 8 and Table 5). Thus, **1**-CN presents a unique case, as the π-acidic nature of the CN$^-$ ligand supports an Fe≡O π-bond similar to that of **1**-NCMe, whereas its σ-donor properties lead to the least covalent Fe≡O σ-bond among the **1**-X series. This interplay between π-acidity and σ-basicity explains why the ν_{FeO} of **1**-CN is similar to that of the other pseudohalides, even though the basicity of CN$^-$ would be more consistent with a lower-energy Fe≡O vibration.

3.3.3. Assignment of LMCT Transitions. The observation of ν_{FeO}'s for **1**-NCMe, **1**-O$_2$CCF$_3$, and **1**-CN, none of which exhibit CT features in the visible region, can be attributed to excitation in near-resonance with an O^{2-} → Fe^{IV} CT transition in the UV spectral region, and this conclusion is supported by the excitation profile obtained for **1**-NCMe (Figure 6B). This finding calls into question our previous assignment of the visible bands of **1**-N$_3$ and **1**-NCS as O^{2-} → Fe^{IV} CT transitions.[28] This earlier interpretation, while consistent with our previous data, is counterintuitive, as replacement of MeCN with more electron-donating ligands, such as N$_3^-$ and NCS$^-$, should lower the Lewis acidity of the Fe^{IV} center, shifting the O^{2-} → Fe^{IV} CT transitions to higher energies. It is thus possible that the observation of ν_{FeO} for **1**-N$_3$ and **1**-NCS is the result of a near-resonance excitation of an O^{2-} → Fe^{IV} CT transition in the UV spectral region and not of the electronic transition(s) in the visible region. If that were the case, the visible absorption bands could be assigned as N$_3^-$/NCS$^-$ → Fe^{IV} CT transitions. That assignment would be consistent with observation of low-energy CT transitions at ~540 nm, likely N$_3^-$ → Fe^{IV} in nature, for a related complex with an Fe^{IV}–N$_3$ unit but with no oxo ligand, [Fe^{IV}(N$_3$)(Me$_3$cyclamacetate)]$^+$.[72,73] Under that assumption, however, one might expect to observe pseudohalide-related vibrations upon 407-nm excitation, and that is not the case.[28] Because the resonance Raman data do not allow us to unambiguously assign the UV−visible LMCT features of **1**-N$_3$ and **1**-NCS, as well as that of **1**-NCO, which displays a λ_{max} at ~350 nm (Figure 3), we turned to DFT computations to gain further insight into the nature of these absorption bands.

3.3.3.1. TD-DFT and ΔSCF Computations. Because the TD-DFT method was previously used to determine excited-state energies for oxoiron(IV) complexes,[25,64] we used this procedure to predict electronic absorption spectra for **1**-N$_3$, **1**-NCS, **1**-NCO, and **1**-NCMe. Using the experimental transition energies reported for **1**-NCMe as a benchmark,[62] we evaluated the performance of several different functionals for our model of **1**-NCMe (Supporting Information) and determined that the PBE0 hybrid functional afforded transition energies and intensities in best agreement with the experimental data. The computed absorption spectrum of **1**-NCMe displays a low-energy band (band *i*; Figure 9) of moderate intensity that corresponds to the prominent NIR band observed in the experimental spectrum at 824 nm (Figure 2). Consistent with the experimental band assignments,[62,64] the intensity of the computed band *i* largely
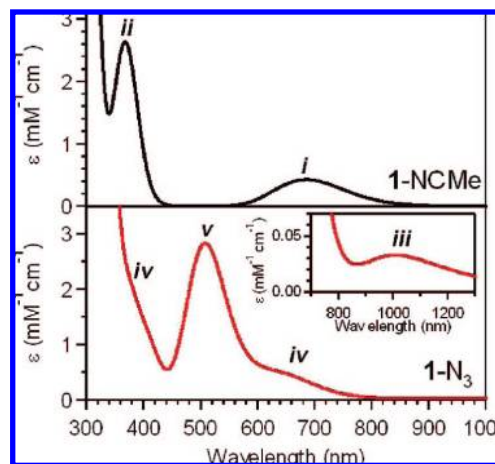

Figure 9. Electronic absorption spectra for **1**-NCMe (top) and **1**-N$_3$ (bottom) obtained by TD-DFT computations.

derives from the d$_{xz/yz}$ → d$_{x^2-y^2}$ transition,[85] with the d$_{xy}$ → d$_{x^2-y^2}$ and d$_{xy}$ → d$_{xz/yz}$ transitions contributing to the lower-energy shoulder (Table 6).

The higher-energy absorption band computed for **1**-NCMe (band *ii*; Figure 9) arises predominantly from O p$_{x/y}$ → Fe^{IV} d$_{xz/yz}$ CT transitions that are mixed with an N$_{TMC}$ p$_{x/y}$ → Fe d$_{x^2-y^2}$ CT transition (state 13, Table 6). The high absorption intensities derive from the large percentage of oxo character in the donor and acceptor MOs (Table 5). The experimental O p$_{x/y}$ → Fe^{IV} d$_{xz/yz}$ CT transition energies were not unambiguously established owing to the overlap of several intense electronic transitions in the UV spectral region. However, a lower limit of 385 nm (>26 000 cm^{-1}) was determined,[62,64] and therefore our TD-DFT computations underestimate the O p$_{x/y}$ → Fe^{IV} d$_{xz/yz}$ CT transition energies to some extent. Nevertheless, as we are most concerned with how these energies are affected upon substitution of the NCMe ligand with a pseudohalide, an absolute agreement between experimental and predicted transition energies is not essential for our analysis.

Because the TD-DFT method reasonably approximated the dominant absorption features for **1**-NCMe, we performed similar computations for **1**-N$_3$, **1**-NCS, and **1**-NCO to determine the energies of the O^{2-} → Fe^{IV} and X$^-$ → Fe^{IV} CT transitions for these complexes. The TD-DFT computed absorption spectrum of **1**-N$_3$, upon which we will focus our discussion, is shown in Figure 9 (bottom), whereas the corresponding spectra for **1**-NCS and **1**-NCO are shown in Figure S8. The LF transitions of **1**-N$_3$ are perturbed relative to those of **1**-NCMe (cf. Figure 9 top and bottom), with the Fe^{IV} d$_{xz/yz}$ → d$_{x^2-y^2}$ and d$_{xy}$ → d$_{x^2-y^2}$ transitions of **1**-N$_3$ being red-shifted (by ~5000 and 2000 cm^{-1}, respectively) and carrying less intensity (Table 6). These calculated spectra are in reasonably good agreement with our experimental observations, as **1**-N$_3$ displays NIR absorption maxima at 850 and 1050 nm (Table 1), red-shifted relative to that of **1**-NCMe (λ_{max} = 824 nm). Furthermore, the NIR features of **1**-N$_3$ are significantly less intense than those of **1**-NCMe (ε = 130 and 400 M^{-1} cm^{-1}, respectively). The perturbations of these d → d transition energies can be understood on the basis of the destabilization of the d$_{xz/yz}$ MOs upon replacement of the NCMe

---

(85) Because the **1**-NCMe complex does not have strict C_{4v} symmetry, the Fe^{IV} d$_{xz}$ and d$_{yz}$ MOs are nondegenerate. However, for most **1**-X complexes, these orbitals have very similar energies and thus will be referred to together unless otherwise noted.

Table 6. TD-DFT Calculated Energies, Percent Contributions from Dominant One-Electron Excitations, and Oscillator Strengths for the Major Electronic Transitions of $[Fe^{IV}(O)(TMC)(NCMe)]^{2+}$ (**1**-NCMe) and $[Fe^{IV}(O)(TMC)(N_3)]^+$ (**1**-N_3) Using the PBE0 Functional

band	state	energy (cm^{-1})^a	f_{osc}	transition^a	%	donor MO	acceptor MO	comments
1-NCMe								
	1	9700	<0.00001	$95\beta \rightarrow 100\beta$	58	Fe d_{xy}	Fe $d_{x^2-y^2}$	Fe^{IV} d $\rightarrow$ d
				$95\alpha \rightarrow 100\alpha$	32	Fe d_{xy}	Fe $d_{x^2-y^2}$	Fe^{IV} d $\rightarrow$ d
	2	12 700	0.00001	$95\beta \rightarrow 99\beta$	82	Fe d_{xy}	Fe d_{xz}	Fe^{IV} d $\rightarrow$ d
	3	12 700	0.00001	$95\beta \rightarrow 98\beta$	81	Fe d_{xy}	Fe d_{yz}	Fe^{IV} d $\rightarrow$ d
i	4	16 200	0.00251	$99\alpha \rightarrow 100\alpha$	42	Fe d_{xz}	Fe $d_{x^2-y^2}$	Fe^{IV} d $\rightarrow$ d
	5	16 500	0.00325	$98\alpha \rightarrow 100\alpha$	45	Fe d_{yz}	Fe $d_{x^2-y^2}$	Fe^{IV} d $\rightarrow$ d
				$97\alpha \rightarrow 100\alpha$	20	N_{TMC} $p_{x/y}$	Fe $d_{x^2-y^2}$	Fe^{IV} d $\rightarrow$ d
ii	13	26 700	0.01625	$97\beta \rightarrow 99\beta$	28	O p_x	Fe d_{xz}	$O^{2-} \rightarrow Fe^{IV}$ CT
				$96\beta \rightarrow 98\beta$	26	O p_y	Fe d_{yz}	$O^{2-} \rightarrow Fe^{IV}$ CT
				$96\alpha \rightarrow 100\alpha$	19	N_{TMC} $p_{x/y}$	Fe $d_{x^2-y^2}$	$N_{TMC} \rightarrow Fe^{IV}$ CT
	14	28 900	0.00676	$96\beta \rightarrow 100\beta$	38	O p_y	Fe $d_{x^2-y^2}$	$O^{2-} \rightarrow Fe^{IV}$ CT
				$97\beta \rightarrow 101\beta$	26	O p_x	Fe d_{z^2}	$O^{2-} \rightarrow Fe^{IV}$ CT
				$98\alpha \rightarrow 100\alpha$	15	Fe d_{yz}	Fe $d_{x^2-y^2}$	Fe^{IV} d $\rightarrow$ d
1-N_3								
iii	1	7800	0.00001	$93\beta \rightarrow 100\beta$	56	Fe d_{xy}	Fe $d_{x^2-y^2}$	Fe^{IV} d $\rightarrow$ d
				$93\alpha \rightarrow 100\alpha$	34	Fe d_{xy}	Fe $d_{x^2-y^2}$	Fe^{IV} d $\rightarrow$ d
	2	10 600	0.00018	$99\alpha \rightarrow 100\alpha$	46	N_3 p_x	Fe $d_{x^2-y^2}$	$N_3^- \rightarrow Fe^{IV}$ CT
				$97\alpha \rightarrow 100\alpha$	28	Fe d_{xz}	Fe $d_{x^2-y^2}$	Fe^{IV} d $\rightarrow$ d
	3	11 800	0.00029	$96\alpha \rightarrow 100\alpha$	32	Fe d_{yz}	Fe $d_{x^2-y^2}$	Fe^{IV} d $\rightarrow$ d
				$98\alpha \rightarrow 100\alpha$	25	N_3 $p_{y/z}$	Fe $d_{x^2-y^2}$	$N_3^- \rightarrow Fe^{IV}$ CT
				$93\beta \rightarrow 99\beta$	22	Fe d_{xy}	Fe d_{xz}	Fe^{IV} d $\rightarrow$ d
	4	14 000	0.00030	$93\beta \rightarrow 99\beta$	65	Fe d_{xy}	Fe d_{xz}	Fe^{IV} d $\rightarrow$ d
	5	14 300	0.00018	$93\beta \rightarrow 98\beta$	75	Fe d_{xy}	Fe d_{yz}	Fe^{IV} d $\rightarrow$ d
iv	11	19 600	0.00180	$96\alpha \rightarrow 101\alpha$	30	Fe d_{yz}	Fe d_{z^2}	Fe^{IV} d $\rightarrow$ d
				$98\alpha \rightarrow 101\alpha$	22	N_3 $p_{y/z}$	Fe d_{z^2}	$N_3^- \rightarrow Fe^{IV}$ CT
	12	20 100	0.00422	$98\alpha \rightarrow 100\alpha$	52	N_3 $p_{y/z}$	Fe $d_{x^2-y^2}$	$N_3^- \rightarrow Fe^{IV}$ CT
				$96\alpha \rightarrow 100\alpha$	28	Fe d_{yz}	Fe $d_{x^2-y^2}$	Fe^{IV} d $\rightarrow$ d
	14	20 600	0.00466	$97\alpha \rightarrow 100\alpha$	32	Fe d_{xz}	Fe $d_{x^2-y^2}$	Fe^{IV} d $\rightarrow$ d
				$99\alpha \rightarrow 100\alpha$	22	N_3 p_x	Fe $d_{x^2-y^2}$	$N_3^- \rightarrow Fe^{IV}$ CT
v	15	22 800	0.01080	$96\beta \rightarrow 98\beta$	54	N_3 $p_{y/z}$	Fe d_{yz}	$N_3^- \rightarrow Fe^{IV}$ CT
				$95\beta \rightarrow 98\beta$	13	O p_y	Fe d_{yz}	$O \rightarrow Fe^{IV}$ CT
	17	23 300	0.02010	$97\beta \rightarrow 99\beta$	53	N_3 p_x	Fe d_{xz}	$N_3^- \rightarrow Fe^{IV}$ CT
				$95\beta \rightarrow 98\beta$	13	O p_y	Fe d_{yz}	$O^{2-} \rightarrow Fe^{IV}$ CT

^{a} The α and β designations correspond to spin-up and spin-down MOs, respectively. For compositions of the MOs referred to in this table, see Tables S16 and S20.

ligand with the N_3^- ligand, as shown in Figure 8. The destabilization lowers the energy gap between the $d_{xz/yz}$ and $d_{x^2-y^2}$ MOs and red-shifts the corresponding d $\rightarrow$ d transition energies.

The TD-DFT computed absorption spectrum of **1**-N_3 also differs from that of **1**-NCMe in that a prominent absorption band is predicted at $\sim$500 nm ($\sim$20 000 cm^{-1}) for the former species (band *v*). This absorption band contains contributions from two electronic transitions (states 15 and 17, Table 6), both of which can be assigned as $N_3^- \rightarrow Fe^{IV}$ CT in nature but also contain a minor $O^{2-} \rightarrow Fe^{IV}$ CT component (Table 6). Notably, all $O^{2-} \rightarrow Fe^{IV}$ CT transitions are blue-shifted relative to those of **1**-NCMe, occurring at $\sim$30 000 cm^{-1} for **1**-N_3 (Table S17), consistent with the higher-lying Fe^{IV} $d_{xz/yz}$ MOs of **1**-N_3 relative to those of **1**-NCMe (Figure 8). Additionally, both the TD-DFT computed absorption spectra of **1**-NCS and **1**-NCO display absorption maxima due to NCO^- and NCS^- to Fe^{IV} CT transitions at 415 and 525 nm, respectively, with $O^{2-} \rightarrow Fe^{IV}$ CT transitions being at higher energies (Figure S8). On the basis of these TD-DFT calculations, the visible absorption features of **1**-N_3, **1**-NCS, and **1**-NCO would seem best assigned as $X^- \rightarrow Fe^{IV}$ CT transitions. This assignment, however, is challenged by our resonance Raman data that reveal iron–oxo but no pseudohalide-related vibrations.

To reconcile these observations and gain further insights into excited-state distortions associated with these CT excited states, we turned to the ΔSCF method for treating excited states, as this procedure allows us to energy-minimize nuclear coordinates

Table 7. DFT-Computed $X^- \rightarrow Fe^{IV}$ and $O^{2-} \rightarrow Fe^{IV}$ CT Transition Energies for $[Fe^{IV}(O)(TMC)(X)]^{2+/+}$ Complexes, Where X = NCMe, NCO^-, NCS^-, and N_3^-

X =	1-NCMe	1-NCO	1-NCS	1-N_3
near-UV λ_{max} (cm^{-1})	>26 000	28 600	25 800	24 600
X^- $2p_y \rightarrow Fe^{IV}$ $3d_{yz}$ (cm^{-1})		21 900	19 600	19 000
X^- $2p_x \rightarrow Fe^{IV}$ $3d_{xz}$ (cm^{-1})		22 400	20 000	19 600
O^{2-} $2p_y \rightarrow Fe^{IV}$ $3d_{yz}$ (cm^{-1})	24 900	27 900	25 600	27 000
O^{2-} $2p_x \rightarrow Fe^{IV}$ $3d_{xz}$ (cm^{-1})	25 200	29 400	25 800	27 100

of select excited states.[48,86] The energies of the $X^- \rightarrow Fe^{IV}$ CT and $O^{2-} \rightarrow Fe^{IV}$ CT transitions obtained by this procedure are in good agreement with both those determined experimentally and those computed using the TD-DFT method, predicting $X^- \rightarrow Fe^{IV}$ CT transitions in the visible region for the pseudohalide complexes (Table 7). Energy minimization of the O^{2-} $p_y \rightarrow Fe^{IV}$ d_{yz} CT state for **1**-NCMe led to a markedly elongated Fe–O distance of 1.88 Å (cf. the equilibrium distance of 1.646 Å), whereas all other structural parameters were essentially unchanged. As illustrated by the MO contour plots in Figure 10, this transition formally transfers an electron from an Fe–O π-bonding MO to the corresponding antibonding MO, so the elongation of the Fe–O bond is expected. We next performed a similar computation to determine the dominant structural distortions associated with the N_3^- $p_{y/z} \rightarrow Fe^{IV}$ d_{yz} CT transition. Surprisingly, the excited-state geometry displayed an Fe–O

(86) Jackson, T. A.; Yikilmaz, E.; Miller, A.-F.; Brunold, T. C. *J. Am. Chem. Soc.* **2003**, *125*, 8348–8363.
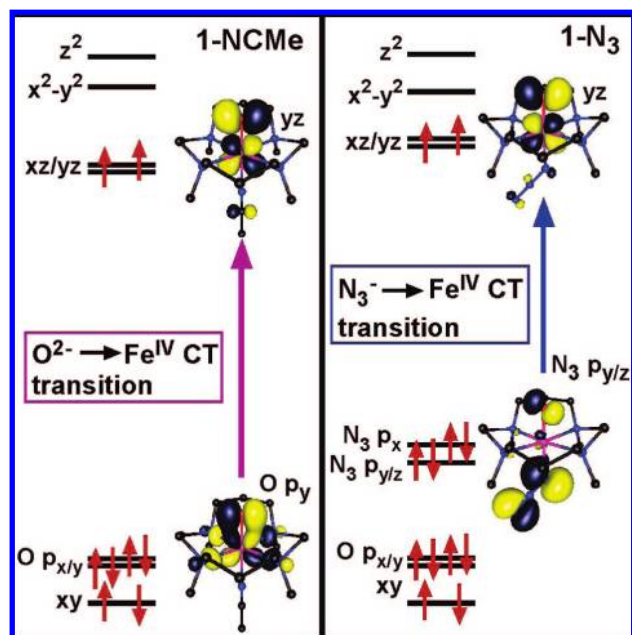
Figure 10. Schematic frontier molecular orbital splitting diagram for $[Fe^{IV}(O)(TMC)(NCMe)]^{2+}$ (**1**-NCMe) and $[Fe^{IV}(O)(TMC)(N_3)]^+$ (**1**-N₃) and contour plots of molecular orbitals involved in LMCT transitions.

distance of 1.85 Å, significantly longer than the ground-state equilibrium distance of 1.68 Å. Furthermore, the Fe–N(N₂) and intra-azide distances were within ±0.02 Å of their ground-state equilibrium values. Thus, these computations demonstrate that the predominant geometric distortion associated with an N_3^- → Fe^{IV} CT transition actually occurs within the Fe–O unit.

This counterintuitive prediction may be rationalized by inspection of the donor and acceptor MOs for the N_3^- $p_{y/z}$ → Fe^{IV} d_{yz} CT transition shown in Figure 10. The N_3^- $p_{y/z}$ MO is localized predominantly on the N_3^- ligand (74% N_3^- character); thus, this MO is essentially nonbonding with respect to the Fe–N₃ unit. In contrast, the acceptor MO is an Fe=O π-antibonding MO (Figure 10) with almost equal iron and oxo character, and a small percentage of N_3^- character ($\sim$10%; Table 5). Thus, an N_3^- $p_{y/z}$ → Fe^{IV} d_{yz} CT transition hardly affects the Fe–N₃ bond but, because this excitation places an electron in an Fe=O π-antibonding MO, weakens the Fe=O bond. Consequently, it may be more accurate to describe the N_3^- → Fe^{IV} CT transition as an N_3^- → Fe^{IV}=O CT transition, as the latter description better reflects the high covalency of the Fe=O unit.

4. Summary and Perspectives

This study presents the spectroscopic characterization of a set of oxoiron(IV) complexes that differ only with respect to the ligand trans to the oxo unit, the most extensive series investigated to date. EXAFS analysis shows that the Fe=O bond length changes little, ranging from 1.64 to 1.68 Å (Table 3). Our DFT calculations (Table 4) support the experimental observations and, like previous calculations on oxoiron(IV) complexes,[63,64,79,80] highlight the covalency of the Fe=O bond. The Fe=O bond is so covalent that axial-ligand-to-metal CT bands observed near 400 nm in $[Fe^{IV}(O)(TMC)(X)]^+$ complexes (X = N₃, NCO, or NCS) are better described as X^- → Fe^{IV}=O CT in character, rather than simply X^- → Fe^{IV}. Thus, the acceptor MO in this CT transition is mainly Fe=O π-antibonding in nature, leading to the observed enhancement of only the
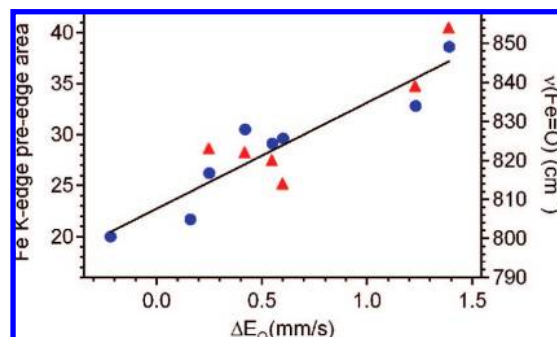

Figure 11. Plot of Fe K-edge pre-edge peak areas (●) and ν(Fe=O) (▲) as a function of Mössbauer quadrupole splitting parameters (ΔE_Q) for the $[Fe^{IV}(O)(TMC)(X)]^+$ complexes.

Fe=O vibration upon excitation of the charge-transfer band. This is fully consistent with the observed Fe=O vibronic structure in d–d transitions of oxoiron(IV) adducts using MCD spectroscopy.[63]

Despite the relative invariance of the Fe=O bond length across the $[Fe^{IV}(O)(TMC)X]^+$ series, there is a perceptible trend, albeit small, of the Fe=O bond length increasing as the axial ligand becomes more basic, particularly when the 1.70 Å Fe=O bond of **1′**-SR is also included. Our calculations show that the σ- and π-donor properties of the trans ligand perturb the relative energies and compositions of the Fe=O σ- and π-antibonding MOs (the Fe^{IV} d_{z^2} and $d_{xz/yz}$ MOs, respectively), with strong donor ligands (i.e., basic ligands) weakening the Fe=O bond (Figure 8). These differences, though not large enough to change the Fe=O bond length significantly, become magnified through the lenses of the spectroscopic methods used in this study because of the sensitivity of these probes to Fe=O bonding. Indeed, it is clear that the donor properties of the trans ligand can exert a considerable influence over all characteristic spectroscopic properties of the oxoiron(IV) unit, including (i) Fe^{IV} d → d transition energies (Figure 2), (ii) XAS pre-edge areas (Table 2), (iii) Mössbauer quadrupole splittings (Table 1), and (iv) the Fe=O stretching frequencies (Table 1). This is in stark contrast to cis ligand effects that have a smaller influence on the spectroscopic properties of the Fe=O unit.[25] For example, the large variation in pre-edge areas observed for the **1**-X series (Table 2) is in contrast to the much smaller range of 25–27 units found for $[Fe^{IV}(O)(TPA)(X)]^{n+}$ (X = MeCN, $CF_3CO_2^-$, Cl^-, and Br^-), where substitutions occur cis to the oxo ligand.[25] Taken together, the different consequences of trans versus cis ligand effects in these model studies are consistent with the observations that Fe^{IV}=O adducts found in nonheme iron enzymes are able to tolerate cis perturbations because the cis position exerts a smaller effect on Fe=O bonding. For example, the halogenase CytC3 employs a chloro ligand cis to the Fe^{IV}=O unit instead of a carboxylate ligand,[11] and a variant of TauD lacking a cis histidine ligand is still able to support an Fe^{IV}=O adduct.[67]

Figure 11 shows the Fe K-edge pre-edge areas plotted against corresponding Mössbauer quadrupole splittings (●), and the line represents the reasonably good correlation between these two sets of parameters. This is the first extensive data set for which it has been possible to establish such a trend. The observed correlation should not be surprising, however, as the magnitude of the observable for both techniques depends on the extent of distortion of the electron distribution from spherical symmetry. The oxo ligand dominates the metal coordination environment and severely distorts it from spherical symmetry, giving rise to

pre-edge areas and quadrupole splittings that are fairly large. The axial ligand can mitigate or enhance the extent of this distortion depending on its σ- and π-donating properties, and this effect accounts for the range of observed pre-edge areas and quadrupole splittings.

There also appears to be some correlation between Fe=O stretching frequencies of the various $[Fe^{IV}(O)(TMC)(X)]^+$ complexes and the Mössbauer quadrupole splittings (Figure 11, ▲), although there are fewer points available (because of our failure to identify the ν_{FeO}'s of **1**-OH and **1**′-SR) and more scatter. In general, the data support the notion that increased basicity of the trans ligand weakens the Fe=O bond.

Our spectroscopic investigations can also be viewed in light of a recent study examining the reactivities of a subset of these complexes, namely **1**-NCMe, **1**-O$_2$CCF$_3$, **1**-N$_3$, and **1**′-SR.[27] These four complexes were compared with respect to their ability to effect oxo transfer to PPh$_3$ and hydrogen atom abstraction from 2,4-di-*t*-butylphenol and dihydroanthracene. Interestingly, while oxo transfer ability increased as expected with greater electrophilicity of the Fe=O unit (i.e., **1**-NCMe > **1**-O$_2$CCF$_3$ > **1**-N$_3$ > **1**′-SR), the trend for hydrogen atom abstraction was exactly the opposite (i.e., **1**-NCMe < **1**-O$_2$CCF$_3$ < **1**-N$_3$ < **1**′-SR). In associated DFT calculations, it was proposed that the counterintuitive and apparently antielectro-philic trend observed for hydrogen atom abstraction could be rationalized by considering how the various axial ligands affect access to the more reactive $S = 2$ excited state of the Fe^{IV}=O unit.[82,87-89] The gap between the $S = 1$ ground state and the $S = 2$ excited state decreases as the extent of charge donation from the trans ligand to the Fe=O unit increases (Figure 8). In principle, this gap should be reflected in the D values of these complexes (Table 1), the magnitude of which depends on the extent of spin−orbit coupling between the $S = 1$ ground state and the $S = 2$ excited state. However, the uncertainty of the D values determined by Mössbauer spectroscopy (± 2 cm^{-1}) allows us to conclude only that the thiolate-ligated complex **1**′-SR has a larger D value and thus a smaller triplet−quintet splitting. The use of alternative methods to more accurately define D for nonheme oxoiron(IV) complexes is currently being investigated.

Intriguingly, the observed hydrogen atom abstraction reactiv-ity trend is *not* reflected in the ν_{FeO} values, where the ordering is **1**-O$_2$CCF$_3$ > **1**-NCMe > **1**-N$_3$. In addition, there is no obvious spectroscopic or computational trend that follows the observed reactivity ordering, which could be a consequence of the relatively small number of complexes used in the reactivity study. Alternatively, the lack of a clear correlation between spectroscopic and reactivity properties could reflect the fact that the spectroscopic parameters are most affected by Fe=O bonding, whereas the triplet−quintet gap involves the d_{xy} and $d_{x^2-y^2}$ orbitals, which do not contribute to the Fe=O bonding interactions. Further studies are clearly warranted to test these alternatives and better define the factors influencing the reactivity of the Fe^{IV}=O unit.

Supporting Information Available: Mössbauer spectra for **1**-N$_3$ (Figure S1), Fe K-edge EXAFS data and fitting analyses for **1**-X complexes (Figures S2, S3, S5, and S6; Tables S1−S3), ESI-MS data for **1**-X complexes (Figure S4), Cartesian coor-dinates and d-based MO compositions for all DFT energy-minimized **1**-X models (Tables S4−S12), details of TD-DFT computations, and plots of predicted absorption spectra for **1**-NCMe, **1**-N$_3$, **1**-NCO, and **1**-NCS (Figures S7 and S8; Tables S13−S20). This material is available free of charge via the Internet at http://pubs.acs.org.

JA8022576

(87) Hirao, H.; Kumar, D.; Que, L., Jr.; Shaik, S. *J. Am. Chem. Soc.* **2006**, *128*, 8590–8606.
(88) Bernasconi, L.; Louwerse, M. J.; Baerends, E. J. *Eur. J. Inorg. Chem.* **2007**, 3023–3033.
(89) Hirao, H.; Que, L., Jr.; Nam, W.; Shaik, S. *Chem.−Eur. J.* **2008**, *14*, 1740–1756.